

## Polarimetric and photometric investigation of a dark globule LDN 1225: distance, extinction law, and magnetic fields

CHAKALI ESWARAI AH,<sup>1,2,3,4</sup> SHIH-PING LAI,<sup>1</sup> YUEHUI MA,<sup>5,6</sup> ANIL K. PANDEY,<sup>7</sup> JESSY JOSE,<sup>8</sup> ZHIWEI CHEN,<sup>9</sup>  
MANASH R. SAMAL,<sup>10</sup> JIA-WEI WANG,<sup>1</sup> SAURABH SHARMA,<sup>7</sup> AND D. K. OJHA<sup>11</sup>

<sup>1</sup>*Institute of Astronomy, National Tsing Hua University (NTHU), 101, Section 2, Kuang-Fu Road, Hsinchu 30013, Taiwan, R.O.C*

<sup>2</sup>*National Astronomical Observatories, Chinese Academy of Sciences, Datun Road, Chaoyang District, Beijing 100101, People's Republic of China*

<sup>3</sup>*CAS Key Laboratory of FAST, NAOC, Chinese Academy of Sciences, Beijing 100101, People's Republic of China*

<sup>4</sup>*Indian Institute of Astrophysics, Koramangala 2nd Block, Bengaluru 560 034, India*

<sup>5</sup>*Purple Mountain Observatory and Key Laboratory of Radio Astronomy, Chinese Academy of Sciences, 2 West Beijing Road, Nanjing 210008, People's Republic of China*

<sup>6</sup>*University of Chinese Academy of Sciences, 19A Yuquan Road, Shijingshan District, Beijing 100049, People's Republic of China.*

<sup>7</sup>*Aryabhata Research Institute of Observational Sciences (ARIES), Manora-peak, Nainital, Uttarakhand-state, 263002, India*

<sup>8</sup>*Indian Institute of Science Education and Research Tirupati, Rami Reddy Nagar, Karakambadi Road, Mangalam (P.O.), Tirupati 517 507, India.*

<sup>9</sup>*Purple Mountain Observatory, Chinese Academy of Sciences, 8 Yuanhua Road, 210034, Nanjing, China*

<sup>10</sup>*Physical Research Laboratory (PRL), Navrangpura, Ahmedabad 380 009, Gujarat, India*

<sup>11</sup>*Department of Astronomy and Astrophysics, Tata Institute of Fundamental Research, Homi Bhabha Road, Mumbai 400 005, India*

### ABSTRACT

We present the results based on the optical *R*-band polarization observations of 280 stars distributed towards the dark globule LDN 1225. *Gaia* data release 2 parallaxes along with the polarization data of  $\sim 200$  stars have been used to (a) constrain the distance of LDN 1225 as  $830 \pm 83$  pc, (b) determine the contribution of interstellar polarization (ISP), and (c) characterize the dust properties and delineate the magnetic field (B-field) morphology of LDN 1225. We find that B-fields are more organized and exhibit a small dispersion of  $12^\circ$ . Using the  $^{12}\text{CO}$  molecular line data from the Purple Mountain Observatory (PMO), along with the column density, dispersion in B-fields, we estimate B-field strength to be  $\sim 56 \pm 10 \mu\text{G}$ , magnetic to turbulence pressure to be  $\sim 3 \pm 2$ , and the mass-to-magnetic flux ratio (in units of critical value) to be  $< 1$ . These results indicate the dominant role of B-fields in comparison to turbulence and gravity in rendering the cloud support. B-fields are aligned parallel to the low-density parts (traced by  $^{12}\text{CO}$  map) of the cloud, in contrast they are neither parallel nor perpendicular to the high-density core structures (traced by  $^{13}\text{CO}$  and  $\text{C}^{18}\text{O}$  maps). LDN 1225 hosts two  $70 \mu\text{m}$  sources which seem to be of low-mass Class 0 sources. The total-to-selective extinction derived using optical and near-infrared photometric data is found to be anomalous ( $R_V = 3.4$ ), suggesting dust grain growth in LDN 1225. Polarization efficiency of dust grains follows a power-law index of  $-0.7$  inferring that optical polarimetry traces B-fields in the outer parts of the cloud.

*Keywords:* Polarization - (ISM:) dust, extinction - ISM: clouds, magnetic fields - local interstellar matter: individual: LDN 1225

### 1. INTRODUCTION

The small, compact, and isolated dark globules known as “Bok globules” (Bok & Reilly 1947), are the potential precursors to the protostars. Initially, Barnard (1927) had prepared a list of such dark regions in the sky and later Lynds (1962) published a catalogue with a larger number of such dark objects. Furthermore, Clemens & Barvainis (1988) have compiled a list of 248 small (mean size  $\sim 4'$ ) and nearby (dis-

tance  $< 1$  kpc) molecular clouds. Subsequent studies have shown that these clouds exhibit signs of star formation such as collimated molecular outflows, compact infrared sources, and very low luminous objects (VELLOs) (Reipurth 1983; Frerking & Langer 1982; Neckel et al 1985; Vrba et al 1986; Neckel et al 1990; Richer et al 2000; Stecklum et al 2007; Reipurth 2008). The characteristics of new born stars will depend on the physical conditions of the molecular cloud core prior to the onset of gravitational collapse.

Turbulence in the dark globules is sub-or trans-Alfvénic (Heyer et al 2008; Franco et al 2010) and the cores embedded in them are characterized with subsonic turbulence (Myers et

al 1983; Goodman et al 1998) such that their effect is inadequate to counteract the gravitational collapse. Therefore, magnetic fields (B-fields) are proposed to play a crucial role in regulating isolated low-mass star formation by controlling the stability and contraction of the cores in these clouds (Mouschovias 1976; Shu 1977; Shu et al 1987). Moreover, it has been shown that B-fields are indeed important in regulating shape of the cloud fragments, guiding accretion flows, directing the outflows, and collimating the jets of the protostars (Vallée 2002; Sugitani et al 2010; Girart et al 2006; Pudritz et al 2007; McKee et al 2007; Galli et al 2009). Here we study the morphological correlations between the cloud and B-fields, and investigate the relative importance of B-fields to turbulence and gravity in LDN 1225 (eg., Myers et al 1991; Ward-Thompson et al 2000; Eswaraiyah et al 2013; Bertrang et al 2014; Kandori et al 2017; Jorquera et al 2018).

The dark globule LDN 1225 (or CB242 or H699 P16) with central coordinates of RA (J2000) =  $23^h 11^m 58^s$  and Dec (2000) =  $+61^\circ 39' 00''$  (or  $l = 111.^\circ 41$ ,  $b = +01.^\circ 02$ ) is located towards the Cepheus OB3 cloud complex (hereafter CepOB3). Based on the derived extinction and distance values of the stars projected toward the cloud, Maheswar & Bhatt (2006) have bracketed the distance of LDN 1225 as  $400 \pm 80$  pc. Nonetheless, our study suggests that, being kinematically associated with CepOB3, LDN 1225 is located at  $830 \pm 83$  pc. A catalog of dust clouds in the Galaxy by Dutra et al (2002) indicates that the spatial extent of LDN 1225 is  $8' \times 4'$ , opacity class as 4 (1 being more lightest and 6 being more darkest; Lynds 1962), and the local standard of rest velocity ( $V_{LSR}$ ) based on CO data as  $-10.9 \text{ km s}^{-1}$  (Clemens & Barvainis 1988). Opacity class 4 (Lynds 1962) is similar to the density class B (A being the most dense and C being the least dense; Hartley et al 1986). Therefore, according to the above opacity classes, LDN 1225 is an intermediate dense dark globule.

In this work, our goal is to investigate whether B-fields support, relative to turbulence and gravity, is important to the formation and evolution of the dark globule LDN 1225. For this purpose, the B-field strength and its pressure, turbulent pressure, ratio of ordered to turbulent component of B-fields, the mass-to-magnetic flux ratio in units of critical value, etc, have been estimated using R-band polarization and CO molecular lines data. Polarimetric data have been used in combination with *Gaia* data release 2 (Gaia Collaboration et al 2018) parallaxes to find the cloud distance, to estimate foreground polarization contribution, and to determine the dust properties and B-fields in LDN 1225. Based on the distances, kinematic information, and the coherent B-fields at small and large scales, the membership of LDN 1225 to the CepOB3 is discussed. The possible correlation between multiple components of polarizations and those of CO gas is discussed. We discuss the properties of two  $70 \mu\text{m}$  sources and

their association with LDN 1225. Optical photometric data have been used to characterize the extinction law in the foreground and cloud mediums. Furthermore, dust polarization efficiency of the dust grains in the dark globule LDN 1225 is studied.

Outline of this paper is as follows. Section 2 describes the observation and data reduction of various observed data along with the archival data sets. Analyses and results are presented in section 3. Discussion based on our results is given in section 4. Summary and conclusions of this work are mentioned in section 5.

## 2. OBSERVATIONS, DATA REDUCTION, AND ARCHIVAL DATA SETS

### 2.1. Polarimetric observations of LDN 1225

Polarimetric observations were carried out on five nights (2010 November 12 and 13, 2010 December 14, and 2013 November 01 and 02), using the ARIES Imaging Polarimeter (AIMPOL; Rautela et al 2004) mounted at the Cassegrain focus of the 104-cm Sampurnanand telescope of the Aryabhata Research Institute of observational sciencES (ARIES), Nainital, India. The observations were carried out in the  $R_c$  ( $\lambda_{Rc_{eff}} = 0.670 \mu\text{m}$ ) photometric band using a small area ( $370 \times 370 \text{ pixel}^2$ ) of the TK 1024  $\times$  1024 pixel<sup>2</sup> CCD camera. Field of view (FOV) of AIMPOL is  $\sim 8$  arcmin diameter on the sky. During the observations the FWHMs of the stellar images vary between  $3 - 5''$ . The read-out noise and gain of the CCD are  $7.0 e^{-1}$  and  $11.98 e^{-1}/\text{ADU}$  respectively. Since AIMPOL does not have the grid, we manually checked for any overlap of ordinary and extraordinary images of the sources. Fluxes of ordinary ( $I_o$ ) and extra-ordinary ( $I_e$ ) beams for all the observed sources with good signal-to-noise ratio were extracted by standard aperture photometry after bias subtraction using the IRAF<sup>1</sup> package. More details on the instrument and the detailed procedures used to estimate the polarization measurements are mentioned in Eswaraiyah et al (2011, and references therein).

All the measurements are corrected for both the instrumental polarization and offset polarization angle by observing unpolarized and polarized standard stars, respectively, from Schmidt et al (1992). As given in the Table 1, our results on the polarized standard stars are in good agreement, within the observational errors, with those from Schmidt et al (1992). Measurements of one unpolarized standard star, HD 21447, as listed in the Table 1, show that the instrumental polarization in  $R_c$ -band is  $\leq 0.1\%$ . This is consistent with the fact that the instrumental polarization of AIMPOL has been monitored since 2004 on various observing nights as a part

<sup>1</sup> IRAF is distributed by National Optical Astronomical Observatories, USA.

of various projects and found to be less than 0.1% in different bands (Rautela et al 2004; Medhi et al. 2008; Eswaraiah et al 2011, 2012; Pandey et al 2013; Eswaraiah et al 2013; Kumar et al. 2014b, 2016; Lee et al 2018).

We have obtained the  $R$ -band polarizations (degree of polarization,  $P_R$  (%), and polarization angle,  $\theta_R$  ( $^\circ$ )) of 280 stars and are listed in Table 2. This table also contains the stellar coordinates and 2MASS photometric data.

Figure 1(a) displays the polarization vector map towards LDN 1225 using  $P_R$  and  $\theta_R$  of 280 stars, which depicts that B-field geometry is not uniform. Of 280, 33 stars are distributed within the  $8'$  diameter field containing the star forming region NGC 7538 which is situated within the Perseus spiral arm of our Galaxy at a distance of 2.65 kpc (Moscadelli et al 2009; Puga et al 2010; Sharma et al 2017). Since these stars are not physically associated with LDN 1225 (located at  $\sim 800$  pc), we exclude them from further analyses. We also omitted 9 stars with NIR-excess ( $[J-H] \geq 1.69 \times [H-K]$ ; see e.g., Eswaraiah et al 2013, 2017) as their polarizations might be consisting of intrinsic components due to asymmetric distribution of material in their circumstellar disks. Remaining 238 stars are used in the further analyses.

## 2.2. Polarimetric observations of several fields covering parts of CepOB3

To understand whether the large scale B-fields of CepOB3 are preserved and have any effect on the small scales of LDN 1225, we also observed 19 additional fields covering different parts of CepOB3 using various polarimeters. Three fields with FOV of  $8'$  diameter were observed in  $R$ -band with AIMPOL on 2016 October 29 and the data are reduced by adopting similar procedures mentioned in the above section 2.1. Eight fields with FOV of  $4'$  diameter were observed in  $R$ -band on five nights (2014 November 19, 20, 25, 26, and 27) using the 2-m telescope of the Inter University Center for Astronomy and Astrophysics (IUCAA), Girawali Observatory, India. The instrument used was the IUCAA Faint Object Spectrograph and Camera (IFOSC) in the polarimetric mode (Sen et al 1994; Ramaprakash et al 1998). Eight fields with FOV of  $4' \times 4'$  are observed on 2015 October 13 with Triple Range Imager and Polarimeter (TRIPOL) mounted on Lulin One-meter Telescope (LOT) at Lulin observatory, Taiwan (Sato et al. in prep.). TRIPOL acquired simultaneous observations in SDSS  $g'$ -,  $r'$ -, and  $i'$ -bands, but we use only the  $r'$ -band data. The measurements from IMPOL and TRIPOL are corrected for both instrumental polarization and offset polarization angles.

Apart from our own observations, we use catalogued  $V$ -band polarization (Heiles 2000) of 16 stars located within the  $5^\circ \times 5^\circ$  field containing CepOB3. We make sure that this sample does not include the stars with possible intrinsic polarization (e.g., Be stars, other emission type stars, young

stellar objects, super-giant, red/blue supergiant, Wolf-rayet stars, etc.) with the help of SIMBAD database.

More details on the results and discussion based on the polarizations of CepOB3 are given in Sections 3.6 and 4.1.

## 2.3. Distances from GAIA DR2

The ESA GAIA mission (Gaia Collaboration et al 2016a,b) data release 2 (Gaia Collaboration et al 2018, hereafter GAIA DR2), provides distance information for stars up to 21 mag. Of the 238 stars which have been used in the present study, 197 have GAIA DR2 parallaxes passing  $10\sigma$  criterion (i.e., parallaxes to their uncertainties,  $\omega/\sigma_\omega \geq 10$ ). The search area of  $1''$  radius around each of the star was used while matching the coordinates of our stars with those of GAIA DR2. Distances of all 197 stars are derived using the relation  $d = (1000/\omega)$  pc (where  $\omega$  is the parallax in milli-arcsecond) and the distance error is estimated by propagating the distance-parallax relation. Based on the asteroseismic data of well-characterized red giant branch (RGB) stars in the *Kepler* field, (Zinn et al 2018, and references therein) have independently confirmed the offset in the parallaxes,  $\sim 52.8 \mu\text{as}$  (micro-arcsecond), of GAIA DR2. However, we have not applied the offset in this study as our main concern is to find the distance of the cloud rather than deriving the distances of individual stars. The distances of the stars are given in the column 9 of Table 2.

## 2.4. Photometric observations towards LDN 1225

Optical photometric observations were performed on 2013 September 6 and 7 using Himalaya Faint Object Spectrograph and Camera (HFOSC) of the 2-m Himalayan Chandra Telescope (HCT) of Indian Astronomical Observatory (IAO), Hanle, operated by Indian Institute of Astrophysics (IIA), India. The central  $2048 \times 2048$  pixel<sup>2</sup> area of the  $2K \times 4K$  CCD was used for data acquisition. The FOV of the instrument is  $10' \times 10'$  area with a pixel size of  $15 \mu\text{m}$  and image plate scale of  $0.293''$  pixel<sup>-1</sup>. Photometric observations in  $BVR$ -bands were performed towards four fields around LDN 1225. We obtained multiple frames in each filters and the total integration time in  $B, V, R$ , and  $I$ -filters was 300, 200, 90, and 90 sec, respectively, in each field. Typical seeing during the observations was  $\sim 1''.5$ . The total area coverage of our optical photometric observations are of  $\sim 17' \times 20'$  around LDN 1225, which is shown with a white box in Figure 1(a). In order to apply atmospheric extinction correction as well as for instrument calibration, we observed the standard star field PG0231 (Landolt 1992) during the nights. PG0231 was observed at various air masses and the nights were photometric. Bias and flat frames were also acquired during the nights.

After bias and flat correction, we stacked all the images of individual fields in each filter. We performed point spread function (PSF) photometry using the DAOPHOT package

in IRAF to derive the instrumental magnitudes. Extinction and instrument coefficients were measured using the instrumental magnitudes and standard star magnitudes of PG0231 field (Landolt 1992). These coefficients were applied to the instrumental magnitudes of LDN 1225 and thus we obtained the final, calibrated photometry. The individual catalogs of four fields were then merged to obtain the final catalog. Typical uncertainty in the photometric calibration is  $\sim 0.05$ ,  $0.03$ ,  $0.02$ , and  $0.02$  mag for the  $B$ ,  $V$ ,  $R$  and  $I$  filters.

Table 3 lists 689 stars with optical ( $BVRI$ ) plus NIR ( $JHK_s$ ; from 2MASS catalog) photometric data with uncertainties less than 0.1 mag. These data have been used in color-color diagrams to investigate the nature of extinction law in the foreground and cloud mediums (cf., Appendix A).

### 2.5. $^{12}\text{CO} (1-0)$ , $^{13}\text{CO} (1-0)$ , and $\text{C}^{18}\text{O} (1-0)$ data from PMO MWISP survey

In order to study the gas kinematics of the cloud LDN 1225, we used the  $^{12}\text{CO}(1-0)$ ,  $^{13}\text{CO} (1-0)$ , and  $\text{C}^{18}\text{O} (1-0)$  molecular line data from the Milky Way Imaging Scroll Painting (MWISP) project<sup>1</sup> using the Purple Mountain Observatory (PMO) Delingha 13.7 m telescope located at Qinghai observing station (see Su et al 2016). LDN 1225 has been observed in November 2015. The MWISP project is a new large-scale survey aiming to perform molecular line observations at the  $J = 1-0$  transition of CO isotopes  $^{12}\text{CO}$ ,  $^{13}\text{CO}$ , and  $\text{C}^{18}\text{O}$  simultaneously. This survey has been specially intended to observe the northern Galactic plane within the Galactic coordinates of  $-10^\circ 25 \leq l \leq 250^\circ 25$  and  $-5^\circ 25 \leq b \leq +5^\circ 25$ , and several other regions of interests. One of the main goals of the MWISP project is to investigate the physical properties of molecular clouds along the northern Galactic plane. The beam sizes are about  $49''.8$  and  $51''.3$  at 115.3 GHz and 110 GHz, respectively. The nominal sensitivities (rms level) in the brightness temperature are 0.47 K in  $^{12}\text{CO}$  at the velocity resolution of  $0.159 \text{ km s}^{-1}$  and 0.26 K in  $^{13}\text{CO}$  and  $\text{C}^{18}\text{O}$  at the velocity resolution of  $\sim 0.167 \text{ km s}^{-1}$ . The resultant data cubes have a FOV of  $30' \times 30'$  and a beam size of  $\sim 53''$ . Our target LDN 1225 is located within the MWISP survey area data of CepOB3. More details on the instrument, data reduction, and analysis procedures can be found at Gong et al (2016) and Su et al (2017).

## 3. ANALYSES AND RESULTS

### 3.1. Distribution of polarization measurements

Figure 2 plots the  $P_R$  versus  $\theta_R$  for 238 stars. The  $\theta_R$  values increase from  $\sim 50^\circ$  to  $\sim 75^\circ$  as a function of increase in  $P_R$  from  $\sim 1\%$  to  $\sim 2\%$ . Beyond which,  $P_R$  increases up to

$\sim 5\%$  while the  $\theta_R$  values are distributed between  $\sim 75^\circ$  and  $\sim 110^\circ$ . To probe the B-field orientation of LDN 1225 we require background (hereafter BG) stars. For this, we need to identify and exclude the FG stars and stars that are not physically associated with the local arm in which LDN 1225 is located. Though, there exist two clear distributions in  $P_R$  versus  $\theta_R$  diagram (separated at  $P_R = 2\%$  and  $\theta_R = 75^\circ$  shown with dashed lines in Figure 2, also see Figure 1(a)), identification of stars belonging to each distribution will be difficult. This can be overcome by knowing the stellar distances, cloud distance, and by classifying the entire sample into FG and BG stars based on their polarizations and distances.

### 3.2. Distance versus polarization plots and distance estimation of LDN 1225

Nearly 93% (197 out of 238) of the stars with polarization data have distance information satisfying the criterion  $\omega/\sigma_\omega \geq 10$  (cf. section 2.3). This information is highly useful to estimate the accurate distance of the cloud. The basis for the distance determination is the occurrence of an abrupt jump in the level of polarization at the cloud distance. The degree of polarization as a function of distance, in the presence of uniform distribution of material along the line-of-sight and according to the canonical extinction to distance relation of  $\langle A_V/L \rangle \approx 1.8 \text{ mag kpc}^{-1}$  (Whittet 2003)<sup>2</sup>, should exhibit a monotonically increasing trend. However, the presence of a cloud (hence increase in the number density of aligned dust grains of the cloud) along the line-of-sight through which background stellar light passes by would cause an enhanced level of polarization at the cloud distance. As a result, a sudden jump in the level of polarization would prevail at the cloud distance. Any change in the orientation of B-fields can also be witnessed in the distance versus polarization angle plot if the B-fields of the cloud are different from those of the FG medium.

Figures 3(a) and (b), respectively, show the distance versus  $P_R$  and  $\theta_R$  of 197 stars. Both  $P_R$  and  $\theta_R$  seem to increase as a function of distance up to 830 pc. In contrast, beyond 830 pc a sudden jump followed by a scattered distribution in  $P_R$  and a constant trend in  $\theta_R$  can be witnessed. Similarly, Stokes parameters ( $Q_R$  and  $U_R$ ) also exhibit linearly decreasing or increasing trends up to 830 pc and beyond which they exhibit scattered distributions (Figures 3(c) and (d)). These abrupt change in  $P_R$ ,  $\theta_R$ ,  $Q_R$ , and  $U_R$  at 830 pc is attributed to the presence of LDN 1225 at this distance.

Since we have used stars with  $10\sigma$  GAIA DR2 distances in our analyses, the expected measurement uncertainty at 830 pc would be 83 pc (10% of 830 pc). Therefore, we ascer-

<sup>2</sup> This relation is applicable only as a general average for lines of sight close to the plane of the Milky Way and for distances up to a few kiloparsecs from the Sun.

<sup>1</sup> <http://www.radioast.nscd.cn/mwisp.php>



tain the distance of LDN 1225 as  $830 \pm 83$  pc. This value supports the distance estimation of  $730 \pm 120$  pc by other studies (Brunt et al 2003, see also Blaauw et al 1959; Crawford et al 1970; Sargent 1977; Ladd et al 1997; Hartigan et al 2000; Kun et al 2008).

In order to elucidate more on the above distance determination, we plot the differential polarization ( $P_{i+1} - P_i$ ), polarization angle ( $\theta_{i+1} - \theta_i$ ), and Stokes ( $Q_{i+1} - Q_i$  and  $U_{i+1} - U_i$ ) versus distance ( $Distance_{i+1}$ ) parameters as shown in Figure 4. The subscript  $i$  varies from 1 to 196 in the increasing order of distances. Since the number of stars is 197, the total differential measurements would be 196. This plot offers a crucial information on the changes in the patterns of polarization measurements of any star relative to those of an immediate foreground. However, in order to see the clear variations of the parameters at the cloud's distance, we limit the data samples up to 2 kpc and plotted distance in linear scale.

Evidently all the differential parameters exhibit a clear transition from negative to positive (or vice versa) at 830 pc as denoted with a green arrow. Region I is dominated by the FG stars, while regions III and IV are with BG stars. Stars with  $747 (830 - 83) \text{ pc} < Distance_{i+1} < 830 \text{ pc}$  (blue circles) are lying in the region I only, in contrast those with  $830 \text{ pc} < Distance_{i+1} < 913 (830 + 83) \text{ pc}$  (red circles) are clearly distributed in both regions III and IV. This observed feature suggests an evidence for the clear changes in the polarization properties of the stars at 830 pc. These changes we attribute to the presence of cloud LDN 1225 at 830 pc.

### 3.3. Identification of foreground and background stars, and their polarization characteristics

Since the distance of LDN 1225 is constrained as  $830 \pm 83$  pc (above section), we consider 61 stars with distances  $< 830$  pc as foreground stars (hereafter FG) and are mentioned as "FG" in column 10 of Table 2, whereas the 136 stars with distances  $\geq 830$  pc as background stars. However, there exist a star forming region NGC 7538 (situated within the Perseus arm at 2.65 kpc; Moscadelli et al 2009; Puga et al 2010; Sharma et al 2017) lying background to LDN 1225 but projected close ( $\sim 15'$ ) to it. In addition, we note below that there exist a background cloud component at the same location of LDN 1225, which is termed as *background cloud* of LDN 1225. In order to examine the physical connection of this component with NGC 7538, we have constructed the position-velocity (PV) plots along the two cuts (cf., Figure 1(b)) using  $^{12}\text{CO}$  data as shown in Figures 5(a) and (b). Evidently, the emissions from LDN 1225 and its *background cloud* are concentrated, respectively, at  $V_{LSR} = -11.2 \text{ km s}^{-1}$  and  $V_{LSR} = -54.5 \text{ km s}^{-1}$ . These two components are located at the same position of the sky (distributed between two horizontal dashed lines) but at different distances (correspond to two dashed vertical lines). Interestingly, the  $^{12}\text{CO}$

emission from NGC 7538 has been widely distributed between  $\sim -40.6 \text{ km s}^{-1}$  and  $\sim -60 \text{ km s}^{-1}$  with a prominent peak emission at  $\sim -56 \text{ km s}^{-1}$ , which is close to the  $-54.5 \text{ km s}^{-1}$  component from the *background cloud*. Moreover, the existence of faint  $^{12}\text{CO}$  emission (green contours around  $V_{LSR} = -54.5 \text{ km s}^{-1}$  in Figures 5(a) and (b)) between *background cloud* and NGC 7538 suggests a physical connection between them. Therefore, hereafter we consider *background cloud* of LDN 1225 is nothing but the region of NGC 7538 lying at 2.65 kpc.

Based on the above paragraph, we consider 18 stars with distances  $> 2.65$  kpc as the background stars of NGC 7538 and are mentioned as "BG-NGC 7538" in the column 10 of Table 2. These stars are excluded from the further analysis, because their polarizations might have comprised of the dust properties and B-field orientations of both clouds NGC 7538 and LDN 1225. The remaining 118 stars having distances between 830 pc – 2.65 kpc, as highlighted within the yellow background in Figure 3, were considered as the true background stars representing the dust properties and B-field orientation of the cloud LN 1225. These stars are mentioned as "BG" in column 10 of Table 2.

Gaussian fits are performed to the polarization distributions of 61 FG and 118 BG stars as shown in the Figure 6. Resultant mean and standard deviation of  $P_{FG}$  and  $\theta_{FG}$  for FG stars are  $1.4 \pm 0.4\%$  and  $61 \pm 11^\circ$  and of  $P_{BG}$  and  $\theta_{BG}$  for the BG stars are  $2.8 \pm 1.0\%$  and  $87 \pm 11^\circ$ , respectively.

### 3.4. Foreground interstellar polarization (ISP)

As shown in Figures 3(c) and (d), the Stokes parameters of 61 FG stars follow a monotonically increasing trend by following a straight line. We took the advantage of this clean set of data to evaluate the foreground interstellar polarization (ISP) component. We performed weighted linear fits (red thick lines) to the distance versus  $Q_R$  and  $U_R$  parameters. The resultant parameters at 830 pc are  $Q_{ISP} = -0.9 \pm 0.1\%$  and  $U_{ISP} = 1.4 \pm 0.1\%$  and the corresponding  $P_{ISP}$  and  $\theta_{ISP}$  values are  $1.7 \pm 0.1\%$  and  $61 \pm 2^\circ$ . These values are considered as the ISP contribution. Similar methodology has been adopted to estimate the ISP contribution and retrieve the intrinsic polarizations of nearby clouds (eg., Eswaraiah et al 2013; Neha et al 2018), B[e] stars (eg., Lee et al 2018), and Supernova (Kumar, B., et al. under review).

### 3.5. Foreground polarization correction to infer B-field structure in LDN 1225

In order to retrieve the true polarization contributions from the cloud LDN 1225, we subtract ISP Stokes parameters ( $Q_{ISP} = -0.9 \pm 0.1\%$ ,  $U_{ISP} = 1.4 \pm 0.1\%$ ) vectorially from those ( $Q_{BG}$  and  $U_{BG}$ ) of 118 BG stars and obtained intrinsic Stokes parameters ( $Q_C$  and  $U_C$ ) of the cloud using the

following relations.

$$Q_C = Q_{BG} - Q_{ISP} \quad (1)$$

$$U_C = U_{BG} - U_{ISP} \quad (2)$$

We then estimate

$$P_C = \sqrt{Q_C^2 + U_C^2} \quad (3)$$

$$\theta_C = 0.5 \arctan(U_C/Q_C). \quad (4)$$

Here, the subscript ‘C’ stands for the cloud, LDN 1225, component. The  $P_C$  values lie between 0.3% – 6.8%, with a Gaussian mean and dispersion of  $2.4 \pm 1.0\%$ . The  $\theta_C$  values lie between  $63 - 128^\circ$ , with a Gaussian mean and dispersion of  $106 \pm 11^\circ$ . This small dispersion in polarization angles implies an uniform B-field orientations within the parts of the cloud. The Gaussian fits to the  $P_C$  and  $\theta_C$  are shown in Figures 7(a) and (b).

In order to test if ISP has any significant impact on the cloud polarization components, we have constructed the histograms of  $\Delta(P) = P_C - P_{BG}$  and  $\Delta(\theta) = \theta_C - \theta_{BG}$  as shown in Figures 7(c) and (d). The Gaussian fit resultant mean and dispersion of  $\Delta(P)$  are  $-0.5\%$  and  $0.6\%$  and similarly the mean and dispersion of  $\Delta(\theta)$  are  $14^\circ$  and  $4^\circ$ , respectively. This implies that the FG medium has a depolarization effect by  $-0.5\%$  on the cloud’s polarization and a systematic rotation effect by  $14^\circ$  on the cloud’s B-field component.

Figure 1(b) displays the B-field morphology of the LDN 1225 region based on the polarization measurements ( $P_C$  and  $\theta_C$ ) of 118 BG stars as depicted with yellow vectors. It should be noted here that these measurements are corrected for ISP contribution. Based on the  $^{12}\text{CO}$  data, the position angle of the major axis of LDN 1225 is found to be  $\sim 102^\circ$  (depicted with a white dashed ellipse in Figure 1; see Section 4.5 and Table 5) and the mean B-field orientation inferred by optical polarimetry ( $\theta_C$ ) of the globule is  $106 \pm 11^\circ$ . This implies that the cloud structure (major axis of the globule) is nearly aligned parallel to the B-fields. This morphological correlation between the cloud structure and B-fields manifests an important role of B-fields in the formation of the globule, detailed discussion on which will be given in Section 4.5.

The B-field orientation of LDN 1225, inferred from mean  $\theta_C = 106 \pm 11^\circ$ , is offset by  $38^\circ$  from the position angle,  $68^\circ$ , of the Galactic plane (GP) at  $b = 1.22^\circ$  (white line in Figures 1(a) and (b) and dashed vertical line in Figure 6(b)). Nonetheless, within the error, the foreground component (mean  $\theta_{FG} = 60 \pm 11^\circ$ ) is parallel to the GP component suggesting that the dust grains of the FG medium are aligned by the local B-fields that are parallel to the GP.

### 3.6. Polarizations of FG and cloud mediums of CepOB3 based on optical polarimetry

By adopting the same distance criteria as of LDN 1225, we identify FG and BG stars in 19 fields of CepOB3 (Section 2.2). Furthermore, assuming that LDN 1225 and CepOB3 share a common ISP contribution (cf. Section 3.5), we correct for it from the polarizations of BG stars and then derive the cloud polarizations of 19 fields of CepOB3. The resultant weighted mean polarizations of foreground and cloud mediums of these 19 fields and their central coordinates, number of stars in each field, and the instrument (or) source used are given in Table 4.

Similarly, V-band polarizations of 15 stars, distributed within the  $5^\circ \times 5^\circ$  area of CepOB3, are extracted from (Heiles 2000) catalog. Of these, 9 are FG and 6 are BG stars according to their distances from GAIA DR2 as well as our analyses concerning the identification of FG and BG stars (eg., Section 3.3). Their coordinates, HD numbers, and polarizations are given in Table 4.

A detailed discussion on the B-field morphologies of FG and cloud mediums of CepOB3 are given in Section 4.1.

### 3.7. Gas velocity dispersion and number density in LDN 1225 using PMO CO data

In order to evaluate the relative importance of B-field to turbulence and gravity, we need to estimate the B-field strength and its pressure. For this, we extract gas velocity dispersion ( $\delta_{V_{LSR}}$ ) and number density ( $n(\text{H}_2)$ ) from the  $^{12}\text{CO}(1-0)$  molecular line data from the PMO MWISP project.

Figure 8 show the  $^{12}\text{CO}(1-0)$  total integrated intensity, velocity, and velocity dispersion maps. These maps were constructed using the velocity channels ranging from  $\sim -13 \text{ km s}^{-1}$  to  $\sim -3 \text{ km s}^{-1}$ , and having the brightness temperature ( $T_b$ ) above 3 times of the rms noise. This selection criterion on the range of velocity channels excludes CO emission from the background cloud NGC 7538 (at  $\sim -54.5 \text{ km s}^{-1}$ ; cf., Figures 5(a) and (b)).

Using CASA software, a two-dimensional Gaussian is fitted to the CO velocity integrated intensity map of LDN 1225 and the resultant spatial extents of major and minor axes, and the position angle of the major axis are  $8'6 \pm 0'2$ ,  $4'3 \pm 0'1$ , and  $102^\circ \pm 1^\circ$ , respectively, and are represented with a black dashed ellipse in Figure 8. These values are consistent with those ( $8'4$ ,  $4'2$ , and  $102^\circ$ ) derived from FCRAO CO data as given in the vizier catalog<sup>3</sup>.

The mean integrated intensity ( $W(\text{CO})$ ) distributed within the extent of LDN 1225 (black ellipse, Figure 8) is  $17 \pm 4 \text{ K km s}^{-1}$ . Using the CO-to- $\text{H}_2$  conversion factor,  $X \equiv N(\text{H}_2)/W(\text{CO}) = (2.0 \pm 0.6) \times 10^{20} \text{ cm}^{-2} (\text{K km s}^{-1})^{-1}$  (Bolatto et al 2013, see also Dame et al 2001 and Sofue et al 2016), the mean column density  $N(\text{H}_2)$  is estimated as  $(3.4 \pm 1.3) \times 10^{21} \text{ cm}^{-2}$ . Assuming the diameter of minor axis,  $4'3 \pm 0'1$  (equivalent

<sup>3</sup> Available at <http://cdsarc.u-strasbg.fr/viz-bin/Cat?J/ApJS/144/47>

to  $1.04 \pm 0.02$  pc at 830 pc), as the thickness of LDN 1225, the mean number density,  $n(H_2)$ , is  $(1.1 \pm 0.4) \times 10^3 \text{ cm}^{-3}$ .

Gaussian fit to the  $^{12}\text{CO}$  mean  $T_b$  versus  $V_{LSR}$  spectrum over an entire region of LDN 1225 resulted a gas velocity dispersion  $\sigma_{V_{LSR}} = 0.88 \pm 0.01 \text{ km s}^{-1}$ . In addition, the fitted values of  $V_{LSR}$  and  $T_b$  are  $-11.08 \pm 0.01 \text{ km s}^{-1}$  and  $4.96 \pm 0.04 \text{ K}$ , respectively.

### 3.8. B-field strength in LDN 1225

Using the dispersion in the B-fields  $\sigma_{\theta_c} = 11.4 \pm 0.3^\circ$  (cf. Section 3.5), gas velocity dispersion  $\sigma_{V_{LSR}} = 0.88 \pm 0.01 \text{ km s}^{-1}$  (cf. Section 3.7), and the mean number density  $n(H_2) = (1.1 \pm 0.4) \times 10^3 \text{ cm}^{-3}$  (cf. Section 3.7) for LDN 1225, we estimate B-field strength using the Davis-Chandrasekhar-Fermi method (more commonly referred to as the Chandrasekhar-Fermi (CF) method; Davis 1951; Chandrasekhar & Fermi 1953):

$$B = Q \sqrt{4\pi\rho} \left( \frac{\sigma_{V_{LSR}}}{\sigma_{\theta_c}} \right). \quad (5)$$

The mass density  $\rho = n(H_2) m_H \mu_{H_2}$ , where  $n(H_2)$  is the hydrogen volume density,  $m_H$  is the mass of the hydrogen atom, and  $\mu_{H_2} \approx 2.8$  is the mean molecular weight per hydrogen molecule which includes the contribution from helium. The correction factor  $Q = 0.5$  is included based on the studies using synthetic polarization maps generated from numerically simulated clouds (Ostriker et al 2001) which suggest that for  $\sigma_\theta \leq 25^\circ$ , B-field strength is uncertain by a factor of two. The estimated B-field strength is  $56 \pm 10 \mu\text{G}$ . Implications based on the relative importance of B-field to turbulent pressure in the formation and evolution of the globule LDN 1225 is discussed in Section 4.2.

## 4. DISCUSSION

### 4.1. Association of LDN 1225 with CepOB3

Based on a detailed comparisons of  $V_{LSR}$ , distance, and B-fields of LDN 1225 with those of CepOB3, we discuss whether LDN 1225 is associated with CepOB3. According to the  $^{12}\text{CO}$  and  $^{13}\text{CO}$  data (from PMO MWISP) of LDN 1225, the mean  $V_{LSR}$  values are  $-11.08 \pm 0.01$  and  $-11.12 \pm 0.02 \text{ km s}^{-1}$ , respectively. These values are consistent with the mean  $V_{LSR}$  of  $-11.2 \text{ km s}^{-1}$  of a number of dark globules, namely, LDN 1210, LDN 1216, LDN 1218, LDN 1220, LDN 1227, LDN 1232, etc (Yonekura et al 1997), which are part of CepOB3. Similarly, several dense clumps of CepOB3 such as LDN 1211, Cep A, Cep B, Cep C, Cep E, and Cep F are also found to have  $V_{LSR}$  values with in a range of  $-8$  to  $-12 \text{ km s}^{-1}$  (Sargent 1977; Yu et al 1996). These inferences suggest that LDN 1225 is kinematically associated with the CepOB3.

As per our present work, LDN 1225 is located at the distance of  $830 \pm 83$  pc (c.f., section 3.2), which is consistent

with the distance 700 pc assigned to LDN 1225 assuming its association with CepOB3 (Sargent 1977; Dame et al 1987; Launhardt et al 1997). The calibrated distance of CepOB3 via principal component analysis (under the assumption of an universal relationship between velocity dispersion and spatial scale within the clouds) on the Five College Radio Astronomy Observatory (FCRAO) Outer Galaxy Survey (OGS) CO data is  $730 \pm 120$  pc (Brunt et al 2003). Using the methanol maser parallaxes, the distance of Cep A is ascertained to be  $700 \pm 40$  pc (Moscadelli et al 2009). This distance value is consistent with those quoted in other studies (Blaauw et al 1959; Crawford et al 1970; Sargent 1977; Ladd et al 1997; Hartigan et al 2000; Kun et al 2008). Therefore, LDN 1225, located at  $830 \pm 83$  pc, is spatially and kinematically associated with the CepOB3.

Furthermore, using the polarization observations of 19 fields (Figure 9(a)), we compare the B-fields in the FG and cloud mediums of CepOB3 with those of LDN 1225 to test if the large scales B-fields are preserved at smaller scales. B-field orientations of FG and cloud mediums of CepOB3, using our observations as well as Heiles (2000) data (cf., Section 3.6), are shown in Figures 9(b) and (c). The weighted mean B-field orientation for the FG medium of CepOB3 is  $67^\circ$  with a standard deviation of  $26^\circ$  (Figure 9(b)), while for LDN 1225 derived as  $61^\circ$  with a standard deviation of  $11^\circ$  (cf., Section 3.3). This implies that the B-fields in the FG mediums of both LDN 1225 and CepOB3 are nearly similar, and are dominated by the GP component of  $68^\circ$ . Similarly, the weighted mean B-field orientation in CepOB3 is  $113^\circ$  with a standard deviation of  $29^\circ$  (as shown in Figure 9(c)), while that for LDN 1225 is  $106^\circ$  with a standard deviation of  $11^\circ$  (cf. Section 3.5). This result again suggests that, within the uncertainty, the mean B-fields in CepOB3 and LDN 1225 are similar implying that B-fields at the small scales of LDN 1225 are inherited from those at large scales of CepOB3. Hence, these large scale B-fields of CepOB3 could be important in governing the formation and evolution of LDN 1225.

Therefore, in conclusion, LDN 1225 is spatially, kinematically, and magnetically has similar characteristics as those for CepOB3, thereby confirming its association with CepOB3.

### 4.2. Cloud stability

To understand the importance of B-fields with respect to turbulence, we estimate the magnetic pressure and turbulent pressure using the relations  $P_B = B^2/8\pi$  and  $P_{turb} = \rho\sigma_{turb}^2$  (where  $\sigma_{turb} = \sigma_{V_{LSR}}$ ) as  $(12 \pm 5) \times 10^{-11} \text{ dyn cm}^{-2}$  and  $(4 \pm 1) \times 10^{-11} \text{ dyn cm}^{-2}$ , respectively. The mean  $P_B/P_{turb}$  is estimated to be  $3 \pm 2$ , suggesting that dominant role of B-fields over turbulence.

To infer the importance of B-fields with respect to gravity, we estimate the mass-to-magnetic flux ratio in units of crit-

ical value using the following relation (Crutcher et al 2004; Chapman et al 2011),

$$\mu = \frac{(M/\phi)}{(M/\phi)_{crit}} = 7.6 N_{\parallel}(H_2)/B_{tot}, \quad (6)$$

where  $N_{\parallel}(H_2)$  is the column density, in units of  $10^{21}$  cm<sup>2</sup>, along the magnetic flux tube and  $B_{tot}$  is the total B-field strength in  $\mu$ G. Critical mass-to-flux ratio,  $(M/\phi)_{crit} = 1/\sqrt{4\pi^2 G}$  (Nakano et al 1978), corresponds to the stability criterion for an isothermal gaseous layer threaded by the perpendicular B-fields. The cloud region with  $(M/\phi) > (M/\phi)_{crit}$  i.e.,  $\mu > 1$  will collapse under its own gravity and cloud is considered to be supercritical. The cloud with  $\mu < 1$  will be in a subcritical state because of the major support rendered by B-fields. Because of the projection effects between  $N_{\parallel}(H_2)/B_{tot}$  and the actual measured  $N(H_2)/B_{\parallel}$  (where  $B_{\parallel}$  is the plane-of-the-sky B-field strength), B-fields parallel to the cloud structure, and assuming random orientation of B-fields with respect to the line of sight, the actual value of  $\mu$  becomes  $(3/4)\mu_{obs}$  (PlanckCollaboration et al 2016, see their Appendix D.4<sup>4</sup>). Therefore, equation (6) can be re-written as  $\mu = 5.7 N(H_2)/B_{\parallel}$ . Using the  $N(H_2) = (3.4 \pm 1.3) \times 10^{21}$  cm<sup>-2</sup> (cf. Section 3.7) and  $B_{\parallel} = 56 \pm 10 \mu$ G (cf. Section 3.8) for LDN 1225,  $\mu$  is estimated to be  $0.35 \pm 0.15$ . This value suggests that LDN 1225 is magnetically subcritical implying strong support by the B-fields, at least, for the outer low-density parts where optical polarimetry is reliable. However, the situation at relatively high dense regions may be different because of the dominance of gravity.

Based on the NH<sub>3</sub> observations of LDN 1225 by Scappini et al (1996), the peak emission occurs at  $V_{LSR} = -11.5 \pm 0.1$  km s<sup>-1</sup>, with a line width  $\Delta_V = 0.8 \pm 0.1$  km s<sup>-1</sup>. They consider LDN 1225 as an inactive globule. However, as per the IRAS Serendipitous Survey Catalog (Kleinmann et al 1986), within the 8' diameter, LDN 1225 hosts IRAS source IRAS 23094+6122 (see also Maheswar et al 2006). Additionally, in this study, based on mid-infrared (MIR) and far-infrared (FIR) images, we find that LDN 1225 hosts two bright MIR YSOs and two *Herschel*/PACS 70  $\mu$ m sources (cf., Section 4.6). These sources are located in the dense parts of LDN 1225, suggesting LDN 1225 is not a quiescent cloud but on the verge of collapse and forming stars.

#### 4.3. Structure function analysis and the ratio of turbulent-to-order B-field strength

Structure function analysis (or angular dispersion function) has been used to derive the ratio of turbulent-to-order B-

field strength ( $\langle B_t^2 \rangle^{1/2}/B_o$ ). To separate the turbulent components from those of non-turbulence, we plotted  $\langle \Delta\theta^2(l) \rangle^{1/2}$  (Falceta-Gonçalves et al 2008; Franco et al 2010; Poidevin et al 2010; Santos et al 2012; Eswaraiyah et al 2013; Franco & Alves 2015; Santos et al 2016), the square root of the second-order structure function or angular dispersion function (ADF)<sup>5</sup>, as a function of distance ( $l$ ) as shown in Figure 10. We used the polarization angles ( $\theta_C$ ) of 118 BG stars to compute  $\langle \Delta\theta^2(l) \rangle^{1/2}$ , which depicts how the dispersion of the polarization angles changes as a function of the length scale in LDN 1225.

The square of the dispersion function can be approximated as follows (Hildebrand et al 2009):

$$\langle \Delta\theta^2(l) \rangle_{tot} - \sigma_M^2(l) = b^2 + m^2 l^2, \quad (7)$$

where  $\langle \Delta\theta^2(l) \rangle_{tot}$  is the dispersion function computed from the data. The quantity  $\sigma_M^2(l)$  is the measurement uncertainties, which is simply the average of the variances on  $\Delta\theta(l)$  in each bin. The quantity  $b^2$  is the intercept of a straight line fit to the data (after subtracting  $\sigma_M^2(l)$ ). Hildebrand et al (2009) have derived the equation for  $b^2$  to find the ratio of turbulent to the large-scale magnetic field strength:

$$\frac{\langle B_t^2 \rangle^{1/2}}{B_o} = \frac{b}{\sqrt{2-b^2}}, \quad (8)$$

In Figure 10, we show the ADF versus displacement using  $\theta_C$  of 118 BG stars for LDN 1225 region. The errors in each bin are similar to the size of the symbols. Each bin denotes  $\sqrt{\langle \Delta\theta^2(l) \rangle_{tot} - \sigma_M^2(l)}$  i.e., the ADF corrected for the measurement uncertainties. Bin widths are in logarithmic scale. Only the first five data points were used in the linear fit to ensure that the length scale ( $l$ ) in the fit (0.003 to 0.5 pc) is greater than the turbulent length scale ( $\delta$ ) (which is of the order of 1 milli-parsec (mpc) or 0.001 pc; eg., Li et al 2008) and much shorter than the cloud length scale ( $d \sim 1$  pc) i.e.,  $\delta < l \ll d$ , to the data (equation (7)) versus distance squared. The fitted function is denoted with a thick dotted line. Since our optical polarimetric observations have a low resolution due to the available limited number of point sources, the minimum length we probed is  $\simeq 31$  mpc. The turbulent contribution to the total ADF is determined by the zero intercept of the fit to the data at  $l=0$ . The net turbulent component,  $b$ , is estimated as  $10 \pm 2^\circ$  (or  $0.17 \pm 0.04$  rad). This dispersion value ( $10 \pm 2^\circ$ ) estimated using structure function analysis is nearly similar to the dispersion in  $\theta_C$  obtained using Gaussian fit ( $\sigma_{\theta_C} = 11^\circ$ ; Section 3.5). The ratio of the turbulent to large-scale magnetic field strength ( $\sigma(\theta) = \langle B_t^2 \rangle^{1/2}/B_o$ ) is computed using equation (8)

<sup>4</sup> In order to correct for the projection effects on the estimated mass-to-flux ratio (in critical units), a factor 1/2 is valid for a spheroid cloud, 1/3 for an oblate spheroid flattened perpendicular to the B-fields, and 3/4 for a prolate spheroid elongated along the B-fields (similar to our case).

<sup>5</sup> The angular dispersion function (ADF) is defined as the square root to the average of the squared difference between the polarization angles measured for all pairs of points ( $N(l)$ ) separated by a distance  $l$ .



as  $0.12 \pm 0.03$ . This suggests that the turbulent component of the field is very small compared with the non-turbulent ordered B-field component, i.e.,  $B_t \ll B_o$ . This suggests that large scale ordered B-fields are dominant over the turbulent component in the LDN 1225.

#### 4.4. Correlations among the observed multiple components in CO gas and B-fields

The CO mapping with 1.2 m telescope of the Center of Astrophysics, was carried out towards the Perseus arm covering the CepOB3, Cas A and NGC 7538 (Ungerechts et al 2000). Their survey revealed that  $V_{LSR}$  of the local arm lie between  $+5$  and  $-25$  km s<sup>-1</sup>, which is clearly separated kinematically from the distant Perseus arm whose  $V_{LSR}$  lie between  $-45$  and  $-80$  km s<sup>-1</sup> with a mean  $V_{LSR} \sim -54.5$  km s<sup>-1</sup>. It is worth stating here that there exist an emission free irregular band between  $\sim -45$  km s<sup>-1</sup> and  $-20$  km s<sup>-1</sup> in the PV diagram (Ungerechts et al 2000, see their Figures 2a and 2b), suggesting a dearth of material within the inner arm. This is also true from PV cuts on <sup>12</sup>CO data towards a small area containing LDN 1225 as shown in Figure 5. This result would also suggest the absence of an additional cloud component with a significantly different B-field orientation within the inner arm. Therefore, it is worth to claim that  $\theta_R$  values lying between  $\sim 70 - \sim 100^\circ$  (Figure 3(b)) and having distances between 830 pc – 2.65 kpc may correspond to the B-fields of LDN 1225, and hence the dispersion in the  $\theta_R$  values is due to the turbulence with in the cloud. However, a larger dispersion in the corresponding  $P_R$  values spanning a range of  $\sim 1.5 - \sim 5\%$  (Figure 3(a)) is owing to different optical depths, causing different amounts of polarization values as traced by the background stars lying at different parts of the cloud.

Furthermore, the local arm possesses three gas components centered around  $\sim +5$ ,  $\sim -5$ , and  $\sim -10$  km s<sup>-1</sup>. The  $-10$  km s<sup>-1</sup> component with a relatively dense gas is attributed to the CepOB3 located at  $\sim 800$  pc, whereas the other two components with less dense gas may correspond to the diffuse foreground dust layers located between our Sun and CepOB3. It is interesting to state that distribution of gas with the components  $-5$  km s<sup>-1</sup> and  $-10$  km s<sup>-1</sup> exhibits a continuous spread implying the presence of uniformly distributed tenuous medium up to the CepOB3. This is further corroborated from a continuous increase in the level of polarization as a function of distance (cf., Figure 3) as well as from a smooth variation of  $P_R$  with  $\theta_R$  (cf., Figure 2).

Presence of two components can be witnessed in the  $P$  and  $\theta$  distributions of FG and BG stars (Figure 6, sections 3.3 and 3.5). B-field component of the FG medium is oriented along the Northeast–Southwest (with a mean  $\theta_{FG} = 61 \pm 11^\circ$ ), while that of the cloud medium is along East–West (with a mean  $\theta_C = 106 \pm 11^\circ$ ). These two components, with dif-

ferent mean polarization values, are separated at  $P_R = 2\%$  and  $\theta_R = 75^\circ$  (Section 3.1). In summary, our polarization observations revealing two distributions in both degrees of polarization and polarization angles are consistent with two CO cloud components centered around  $\sim -5$  km s<sup>-1</sup> and  $\sim -10$  km s<sup>-1</sup>.

#### 4.5. Geometry of LDN 1225 in <sup>12</sup>CO, <sup>13</sup>CO, and C<sup>18</sup>O molecular lines

Generally the <sup>12</sup>CO emission comes from the tenuous gas distributed in low density parts of the cloud, whereas the <sup>13</sup>CO and C<sup>18</sup>O emissions come from the inner, denser gas. Since LDN 1225 has been observed simultaneously at these three molecular lines, we compare the ambient mean B-fields orientation with the orientations of major axes of LDN 1225 at different length scales and depths. These comparisons would reveal how the B-fields, turbulence, and gravity interact with the cloud material and govern its structure, stability, and contraction at different scales and depths (Eswaraiah et al 2013). The advantage in using molecular lines to determine the cloud structure is that the foreground cloud component will be well separated from that of the background in velocity space.

We have employed CASA 2D Gaussian fitting function on the moment 0 maps of <sup>12</sup>CO, <sup>13</sup>CO, and C<sup>18</sup>O, respectively shown with red, green, and magenta contours in Figure 11, and extracted the spatial extents and position angles of the cloud elongations. The corresponding fitted central coordinates, FWHMs of major and minor axes, and position angles are given in Table 5. Last column gives the offset ( $\Delta(\theta)$ ) between the cloud position angles ( $\theta_{cloud}$ ) traced by three CO lines and mean B-field orientation ( $\theta_C$ , Section 3.5) of LDN 1225.

The  $\Delta(\theta)$  from <sup>12</sup>CO is  $4 \pm 11^\circ$ , implying low density outer parts of the cloud are nearly aligned parallel with the ambient B-fields, suggesting importance of B-fields in governing the cloud structure. However,  $\Delta(\theta)$  values from <sup>13</sup>CO and C<sup>18</sup>O to be  $54 \pm 11^\circ$  and  $52 \pm 14^\circ$ ; indicating that, within the error, the PAs of the denser parts of the cloud are neither parallel nor perpendicular to B-fields. This suggests that B-fields of the low-density outer parts may not equally be important in governing the cloud structure at high-density inner parts; in other words turbulence and gravity might be crucial at these denser parts. In order to shed more light on these, we need to probe the B-fields in the denser parts, using NIR and sub-mm polarimetry.

#### 4.6. Association of MIR and 70 $\mu$ m point sources with LDN 1225

In order to confirm if LDN 1225 is a starless or star forming cloud, we search for the YSOs by examining the multi-wavelengths images of LDN 1225 as shown in the Figure

12. We have identified two MIR (diamonds) and two 70  $\mu\text{m}$  (circles) sources, respectively, in the images of *WISE* 22  $\mu\text{m}$  (Figure 12(b)) and *Herschel*/PACS 70  $\mu\text{m}$  (Figure 12(c)). These sources appear to be part of LDN 1225, because as they are located within the extent and center of the cloud as seen in optical absorption (Figure 12(a)) and dust emission inferred from the column density map<sup>6</sup> (Figure 12(d)). Nonetheless, CO data cubes reveal two overlapping cloud components towards LDN 1225 – one at  $V_{LSR} = -11.2 \text{ km s}^{-1}$  (red contours) and the another at  $V_{LSR} = -54.5 \text{ km s}^{-1}$  (yellow contours) as shown in Figures 12(a) – (d) (see also PV cuts in Figures 5(a) and (b)). Because of this, a confusion prevails on whether YSOs are originally belong to the LDN 1225 or to the background cloud NGC 7538.

To elucidate more on the association of YSOs, we have searched for the  $^{12}\text{CO}$ ,  $^{13}\text{CO}$ , and  $\text{C}^{18}\text{O}$  emissions from LDN 1225 (top panels) and NGC 7538 (bottom panels), especially, at the locations of the YSOs as shown in Figure 13. Evidently, all YSOs are distributed, not only within the emissions from low-density tracers ( $^{12}\text{CO}/^{13}\text{CO}$ ) but also that from dense gas tracer ( $\text{C}^{18}\text{O}$ ) of LDN 1225. Moreover, despite of a small amount of  $^{12}\text{CO}/^{13}\text{CO}$  emission, a complete devoid of  $\text{C}^{18}\text{O}$  emission from NGC 7538 is witnessed at the sites of YSOs. This implies that LDN 1225 comprises of denser gas than background cloud. These results reinforce the fact that LDN 1225 is indeed a star forming dark globule, hosting MIR and 70  $\mu\text{m}$  sources in its denser parts.

#### 4.7. Properties of 70 $\mu\text{m}$ sources

Since 70  $\mu\text{m}$  sources are brighter in FIR and fainter in NIR and MIR wavelengths (cf., Figure 12), their disks may have negligible contribution to the shape of spectral energy distribution (SED) at  $\lambda \leq 100 \mu\text{m}$  (eg., Whitney et al 2005). The main contributor to the SED of 70  $\mu\text{m}$  sources could be from their envelopes. In order to study the nature of these 70  $\mu\text{m}$  sources (cf., Section 4.6 and Figure 13), we have performed aperture photometry on the *Herschel* images as documented in Balog et al (2014) and modified blackbody fitting was performed on the fluxes at 70, 160, 250, and 350  $\mu\text{m}$ <sup>7</sup> as shown in Figure 14(a) and (b).

The computed envelope masses ( $M_{env}$ ), bolometric luminosities ( $L_{bol}$ ), and dust temperatures ( $T_{dust}$ ) are 11  $M_{\odot}$  & 4  $M_{\odot}$ , 5  $L_{\odot}$  & 8  $L_{\odot}$ , and 13 K & 17 K, respectively, for

<sup>6</sup> Column density map has been constructed by fitting the modified blackbody function on the *Herschel* PACS and SPIRE fluxes as described in Appendix D of Eswarajah et al (2017, and references therein). Data have been take from *Herschel* Infrared Galactic Plane Survey (Hi-GAL; Molinari et al 2010).

<sup>7</sup> Fluxes at 500  $\mu\text{m}$  have been excluded, owing to the low-resolution of the 500  $\mu\text{m}$  beam. This is done in order to avoid the biasness in the fitting procedure due to overestimation of fluxes at 500  $\mu\text{m}$  because of source confusion and inclusion of excess background emission.

sources 1 & 2. SED fits suggest that the envelopes of the two 70  $\mu\text{m}$  sources are of low-mass and low-luminous Class 0 protostars.

Furthermore, we have used the above physical parameters of these sources to infer their final evolutionary status based on the  $M_{env}-L_{bol}$  diagram (Figure 15). The location of the two 70  $\mu\text{m}$  sources in comparison to the evolutionary tracks of protostars with different envelope masses and luminosities (André et al 2008, and references therein), suggest that they may evolve into stars with their final masses span over 1  $M_{\odot}$  to 5  $M_{\odot}$  at the end phases of accretion (see the tip of the arrows in Figure 15).

#### 4.8. Are the B-fields important to the Star formation in LDN 1225?

If B-fields are important in a cloud to form the cores via ambipolar diffusion process or strong B-field model (Mouschovias 1976; Shu 1977; Shu et al 1987; Mouschovias 1991; Mouschovias et al 1999) then (i) the B-field structure in the low density subcritical envelope should be aligned with the cloud structure, (ii) high-density core's major axis should be perpendicular to the envelope B-fields, and (iii) B-fields within the core should follow an hour-glass shape if the core is in a supercritical state and collapsing.

The first condition is true in LDN 1225 because the mass-to-magnetic flux ratio in units of the critical value,  $\mu_c$ , is  $< 1$  suggesting that envelope is in a subcritical state (section 4.2) and hence the low-density envelope is strongly supported by B-fields. In addition, being parallel to the low-density parts (section 3.5), B-fields aid the cloud contraction producing elongated core structures perpendicular to them. However, since the core long axis is neither parallel nor perpendicular to the ambient B-fields (section 4.5), the second condition may not be true in LDN 1225.

High density cores are in a super-critical state as they are collapsing to form stars (Section 4.6). Since we have not probed the B-fields at the core scale and have not derived various parameters (B-field strength, B-field pressure, turbulent pressure, mass-to-flux ratio in terms of critical value, etc), the examination of the strong B-field model (third condition) is beyond the scope of this work. Therefore, to shed more light on whether or not the B-fields are important at core scales, we need to probe the B-fields using NIR/sub-mm polarimetry.

#### 4.9. Extinction law

Dust grain mean size distribution can be evaluated by using the parameter  $R_V = A_V/E(B-V)$ , the total-to-selective extinction which is also termed as extinction law (Cardelli et al 1989; Olofsson et al 2010). Though, the mean  $R_V$  for the Milky Way Galaxy is 3.1, it varies from one line of sight to the other. To characterize the extinction law towards LDN 1225, we have used two-color diagrams (TCDs) of the

form  $(V - \lambda)$  versus  $(B - V)$ , where  $\lambda$  is the one of the magnitude in broad-band filters,  $R$ ,  $I$ ,  $J$ ,  $H$ ,  $K_s$ , or  $L$ . These diagrams are usually employed to characterize the extinction law in the foreground and cloud (or stellar cluster) mediums (eg., Pandey et al 2000, 2003; Samal et al 2007; Eswaraiyah et al 2013; Pandey et al 2013; Kumar et al 2014a). Since the distance of LDN 1225 and the number of FG/BG stars are known, as illustrated in Appendix A, we derive the  $R_V$  values for the foreground and cloud mediums. For this purpose we have used the optical and NIR photometric data from Table 3.

Based on the two-color diagrams (Figures 16 and 17) and estimated weighted mean  $R_V$  values (see Appendix A for more details on the Figures and Table), the following points can be made: (a) FG and BG stars of groups I (stars with photometry) and II (stars with photometry plus polarimetry) exhibit conspicuously two different distributions represented by different amount of slopes and  $R_V$  values, (b) within the error,  $R_V$  values of FG (BG) stars belong to the two groups are nearly same and consistent with each other, (c) the extinction law in the foreground medium is normal i.e.,  $R_V \sim 3.1$  characterized with mean dust grain sizes, and (d) the extinction law in the cloud medium is abnormal i.e.,  $R_V \sim 3.4$  characterized with relatively bigger dust grain sizes in the regions of LDN 1225 that we probed with photometry and polarimetry.

Different dust size is found towards different Galactic line of sights. For example, toward the high-latitude translucent molecular cloud direction of HD 210121 (Welty et al 1992; Larson et al 1996),  $R_V$  is 2.1, whereas toward the HD 36982, molecular cloud direction in the Orion nebula, the  $R_V$  values lie between 5.6 – 5.8 (Cardelli et al 1989; Fitzpatrick 1999; Draine 2003). In our work, an abnormal extinction law (with  $R_V \sim 3.4$ ) in LDN 1225 might have produced by the bigger dust grains resulted via dust grain growth by means of dust coagulation or dust accretion processes. These processes could take place in the molecular clouds because of the prevailing different physical conditions such as low temperatures and high density.

#### 4.10. Extinction versus polarization and polarization efficiency

To understand the polarization efficiency of the dust grains of LDN 1225, as illustrated in Appendix B, we estimate the visual extinctions ( $A_V$ ) of the field stars (mainly normal main-sequence stars and giants) of LDN 1225 by dereddening their NIR colors (Table 3) shown in Figure 18. Figure 19(a) shows the  $A_V$  versus  $P_R$  plot of 27 stars (of these 3 FG and 24 BG stars). Polarization values of all the stars (except 2 BG stars) distributed below the observed upper limit polarization relation  $P/A_V < 3\% \text{ mag}^{-1}$  (Serkowski et al 1975) and exhibit a linear trend as a function of extinction.

The polarization efficiency ( $P_R/A_V$ ) of the dust grains of LDN 1225 tends to follow a systematically declining trend as a function of extinction ( $A_V$ ), similar to the other works (e.g., Goodman et al 1995; Gerakines et al 1995; Whittet et al 2008; Eswaraiyah et al 2013; Wang et al 2017), by following a power-law of the form  $P/A_V \propto A_V^{-\alpha}$  shown in Figure 19(b). Weighted power-law fit to the data points of 22 BG stars (3 FG and 2 BG stars are excluded from the fit; see figure caption for more details) satisfies the relation  $P_R/A_V \propto A_V^{-0.7 \pm 0.5}$ . Within the error, the power-law index  $-0.7 \pm 0.5$  is consistent with the index  $-0.7 \pm 0.1$  for the entire molecular cloud complex IC 5146 using  $R_c$  band data (Wang et al 2017),  $-0.8 \pm 0.1$  for Pipe-109 using  $R$ -band data (Alves et al 2014), and  $-0.7 \pm 0.1$  for L2014 using  $H$ -band data (Cashman & Clemens 2014). These reported indices are generally found for the low-density parts of the cloud observed in optical wavelengths, having  $A_V$  values of 1 – 4 mag. However, softer indices ( $-0.3$  to  $-0.5$ ) are found towards the dense parts of the clouds with high extinction regions ( $A_V > 5$  mag) observed in NIR wavelengths (Whittet et al 2008; Jones et al 2015; Wang et al 2017).

The negative index  $-0.7 \pm 0.5$  implies that dust grains at the low-density outer parts result higher polarization efficiency, while those at relatively high-density inner parts result lower polarization efficiency. This is due to the variation of several factors as a function of extinction (Jones 1989; Jones et al 1992; Gerakines et al 1995; Whittet 2005; Whittet et al 2008): (a) the dust grains themselves (size, shape, composition, presence or absence of surface coatings), (b) B-field direction weighted according to the distribution of dust grains along the line of sight, (c) the dust grain alignment efficiency, and (d) the physical conditions of the environment in which dust exist. Since our optical polarimetry is confined to the low-density outer parts of LDN 1225 and due to a small dispersion in the mean B-field orientation of LDN 1225, we interpret that the observed polarization efficiency with an index of  $-0.7 \pm 0.5$  is due to the changes in the properties and alignment efficiency of dust grains as a function of extinction.

The power-law index can also infer whether the observed polarization observations trace the B-fields in the cloud. Ideally, a power-law index of  $-1$  may corresponds to ceasing of dust grain alignment producing null polarization thereby providing no clues about the B-field orientation. However, in this work, the index of  $-0.7$  suggests that the dust grains are still aligned and our optical polarimetry is able to trace the B-fields at relatively less dense, outer parts of the cloud.

## 5. SUMMARY AND CONCLUSIONS

We have performed single  $R_c$ -band polarimetric and multi-band  $(BV(RI)_c)$  photometric observations of the stars distributed towards a dark globule LDN 1225. A total of 280

stars were found to have  $R_C$  polarization data satisfying the  $2\sigma$  criterion and also 689 stars are found to have optical plus 2MASS photometric data with uncertainties less than 0.1 mag. We use multi-wavelength images from DSS, WISE, *Spitzer*, and *Herschel*, parallaxes from GAIA DR2, and CO molecular lines data from PMO. In this work, we investigate the distance of LDN 1225, distribution of dust and B-field orientation as a function of distance, importance of B-fields in the formation and evolution of cloud, and extinction law in the foreground and cloud mediums.

Main results of our study are summarized below:

- Based on the distance versus polarization, polarization angles, and Stokes parameters plots, we ascertain the distance of LDN 1225 as  $830 \pm 83$  pc.
- Total sample with polarization data are classified into foreground (FG) and background (BG) stars, based on the individual stellar distances in comparison to the cloud distance. FG and BG stars exhibit bimodal distributions in both the level of polarizations and polarization angles.
- FG stars exhibit increasing trends in their polarizations and Stokes parameters. We make use of these samples to characterize the interstellar polarization (ISP) contribution and the same is subtracted to infer the B-field geometry of the cloud.
- Using the dispersion in the cloud's B-field orientations, gas velocity, and number density from PMO CO data, we estimate the B-field strength as  $56 \pm 10 \mu\text{G}$ , by using the Davis-Chandrasekhar-Fermi relation. We find that magnetic pressure is 3 times higher than the turbulent pressure, and also that the mass-to-magnetic flux ratio in units of critical value is less than one. These results imply that the dominance of B-fields over turbulence and gravity in the envelope of LDN 1225.
- The morphological correlations between B-fields and cloud geometry at different optical depths, as probed by  $^{12}\text{CO}$ ,  $^{13}\text{CO}$ , and  $\text{C}^{18}\text{O}$  molecular lines, depict that B-fields might not be so important in the core scale of LDN 1225.
- Based on the *WISE* and *Herschel* images along with the CO molecular lines data, we find that LDN 1225 host two MIR and two  $70 \mu\text{m}$  sources thereby reinforcing that LDN 1225 is not a starless but star forming dark globule.
- Structure function analysis suggests that the contribution from the turbulent component of magnetic fields is very small compared with that of the non-turbulent ordered component in LDN 1225.

- B-fields in LDN 1225 remain coherent with the large scale B-fields of CepOB3.
- Using the distance versus polarizations, CO molecular lines data, and B-fields, we infer that LDN 1225 is associated and located at the same distance as CepOB3.
- Using the photometric colors, the extinction law is tested in the foreground and cloud mediums. We find that foreground medium is characterized with the normal extinction law, whereas the cloud medium is with an abnormal extinction law.
- Polarization efficiency of the dust grains of LDN 1225 decline as a function of extinction and yields a power-law exponent of  $-0.7 \pm 0.5$  implying that our optical polarimetry is capable of tracing B-fields in the low-density parts of LDN 1225.

In conclusion, we make use of the polarization and distance information to study the dust distribution and their properties, and B-field orientation of the cloud. This can serve as an important tool to probe the 3D tomography of ISM and B-fields towards the molecular clouds and star forming regions. Photometry has been utilized to investigate the nature of extinction law to characterize the dust properties. Polarimetry along with the molecular lines data serve as an efficient tool to study the correlations between the multiple polarization and cloud components. Multi-wavelength (dust extinction and emission) polarization data, covering different length and density scales, are essential to test the star formation models.

We thank the anonymous referee for his/her constructive comments which have improved the flow and contents of the manuscript. EC and SPL acknowledge support from the Ministry of Science and Technology (MOST) of Taiwan with Grant MOST 106-2119-M-007-021-MY3. This work is supported by National Key R&D Program of China grant No. 2017YFA0402600 and International Partnership Program of Chinese Academy of Sciences grant No. 114A11KYSB20160008. EC is thankful to Prof. Wen-Ping Chen, Prof. G. C. Anupama, and Prof. G. Maheswar for the help, support, encouragement, and fruitful discussions. EC thank Dr. Brajesh Kumar for his careful reading and helpful inputs on the draft.

*Facilities:* ARIES:1m (AIMPOL polarimeter), LO:1m (TRIPOL polarimeter), IUCAA:2m (IFOSC in polarimetric mode - IMPOL), HCT:2m (HFOSC)



## REFERENCES

- Alves, F. O., Frau, P., Girart, J. M., et al. 2014, *A&A*, 569, L1
- André, P., Minier, V., Gallais, P., et al. 2008, *A&A*, 490, L27
- Andre, P., Ward-Thompson, D., & Barsony, M. 2000, *Protostars and Planets IV*, 59
- Balog, Z., Müller, T., Nielbock, M., et al. 2014, *Experimental Astronomy*, 37, 129
- Barnard, E. E. 1927, Chicago: University of Chicago Press, 1927
- Bertelli, G., Bressan, A., Chiosi, C., Fagotto, F., & Nasi, E. 1994, *A&AS*, 106, 275
- Bertrang, G., Wolf, S., & Das, H. S. 2014, *A&A*, 565, A94
- Bessell, M. S., & Brett, J. M. 1988, *PASP*, 100, 1134
- Bolatto, A. D., Wolfire, M., & Leroy, A. K. 2013, *ARA&A*, 51, 207
- Bok, B. J., & Reilly, E. F. 1947, *ApJ*, 105, 255
- Bontemps, S., Andre, P., Terebey, S., & Cabrit, S. 1996, *A&A*, 311, 858
- Blaauw, A., Hiltner, W. A., & Johnson, H. L. 1959, *ApJ*, 130, 69
- Brunt, C. M., Kerton, C. R., & Pomerleau, C. 2003, *ApJS*, 144, 47
- Brunt, C. M., & Kerton, C. R. 2002, *ApJL*, 567, L41
- Cardelli, J. A., Clayton, G. C., & Mathis, J. S. 1989, *ApJ*, 345, 245
- Cashman, L. R., & Clemens, D. P. 2014, *ApJ*, 793, 126
- Chakraborty, A., & Das, H. S. 2016, *Ap&SS*, 361, 321
- Chandrasekhar, S., & Fermi, E. 1953, *ApJ*, 118, 113
- Chapman, N. L., Goldsmith, P. F., Pineda, J. L., et al. 2011, *ApJ*, 741, 21
- Clemens, D. P., & Barvainis, R. 1988, *ApJS*, 68, 257
- Crawford, D. L., & Barnes, J. V. 1970, *AJ*, 75, 978
- Crutcher, R. M., Nutter, D. J., Ward-Thompson, D., & Kirk, J. M. 2004, *ApJ*, 600, 279
- Cutri, R. M., Skrutskie, M. F., van Dyk, S., et al. 2003, *VizieR Online Data Catalog*, 2246
- Dame, T. M., Ungerechts, H., Cohen, R. S., et al. 1987, *ApJ*, 322, 706
- Dame, T. M., Hartmann, D., & Thaddeus, P. 2001, *ApJ*, 547, 792
- Davis, L. 1951, *Physical Review*, 81, 890
- Dobashi, K., Uehara, H., Kandori, R., et al. 2005, *PASJ*, 57, S1
- Draine, B. T. 2003, *ARA&A*, 41, 241
- Dutra, C. M., & Bica, E. 2002, *A&A*, 383, 631
- Eswaraiah, C., Pandey, A. K., Maheswar, G., et al. 2011, *MNRAS*, 411, 1418
- Eswaraiah, C., Pandey, A. K., Maheswar, G., et al. 2012, *MNRAS*, 419, 2587
- Eswaraiah, C., Maheswar, G., Pandey, A. K., et al. 2013, *A&A*, 556, A65
- Eswaraiah, C., Lai, S.-P., Chen, W.-P., et al. 2017, *ApJ*, 850, 195
- Falceta-Gonçalves, D., Lazarian, A., & Kowal, G. 2008, *ApJ*, 679, 537
- Franco, G. A. P., Alves, F. O., & Girart, J. M. 2010, *ApJ*, 723, 146
- Franco, G. A. P., & Alves, F. O. 2015, *ApJ*, 807, 5
- Frerking, M. A., & Langer, W. D. 1982, *ApJ*, 256, 523
- Fitzpatrick, E. L. 1999, *PASP*, 111, 63
- Gaia Collaboration, Prusti, T., de Bruijne, J. H. J., et al. 2016, *A&A*, 595, A1
- Gaia Collaboration, Brown, A. G. A., Vallenari, A., et al. 2016, *A&A*, 595, A2
- Gaia Collaboration, Brown, A. G. A., Vallenari, A., et al. 2018, *A&A*, 616, A1
- Galli, D., Cai, M., Lizano, S., & Shu, F. H. 2009, *Revista Mexicana de Astronomia y Astrofisica Conference Series*, 36, 143
- Gerakines, P. A., Whittet, D. C. B., & Lazarian, A. 1995, *ApJL*, 455, L171
- Girart, J. M., Rao, R., & Marrone, D. P. 2006, *Science*, 313, 812
- Goodman, A. A., Jones, T. J., Lada, E. A., & Myers, P. C. 1995, *ApJ*, 448, 748
- Goodman, A. A., Barranco, J. A., Wilner, D. J., & Heyer, M. H. 1998, *ApJ*, 504, 223
- Gong, Y., Mao, R. Q., Fang, M., et al. 2016, *A&A*, 588, A104
- Güver, T., & Özel, F. 2009, *MNRAS*, 400, 2050
- Hartigan, P., Morse, J., & Bally, J. 2000, *AJ*, 120, 1436
- Hartley, M., Tritton, S. B., Manchester, R. N., Smith, R. M., & Goss, W. M. 1986, *A&AS*, 63, 27
- Hildebrand, R. H., Kirby, L., Dotson, J. L., Houde, M., & Vaillancourt, J. E. 2009, *ApJ*, 696, 567
- Heiles, C. 2000, *AJ*, 119, 923
- Heyer, M., Gong, H., Ostriker, E., & Brunt, C. 2008, *ApJ*, 680, 420
- Heyer, M. H., Brunt, C., Snell, R. L., et al. 1998, *ApJS*, 115, 241
- Jones, T. J., Bagley, M., Krejny, M., Andersson, B.-G., & Bastien, P. 2015, *AJ*, 149, 31
- Jones, T. J. 1989, *ApJ*, 346, 728
- Jones, T. J., Klebe, D., & Dickey, J. M. 1992, *ApJ*, 389, 602
- Jorquera, S., & Bertrang, G. H.-M. 2018, *arXiv:1804.02070*
- Kandori, R., Tamura, M., Kusakabe, N., et al. 2017, *ApJ*, 845, 32
- Kleinmann, S. G., Cutri, R. M., Young, E. T., Low, F. J., & Gillett, F. C. 1986, Tucson, Univ. of Arizona (1986)
- Kumar, B., Sharma, S., Manfroid, J., et al. 2014, *A&A*, 567, A109
- Kumar, B., Pandey, S. B., Eswaraiah, C., & Gorosabel, J. 2014, *MNRAS*, 442, 2
- Kumar, B., Pandey, S. B., Eswaraiah, C., & Kawabata, K. S. 2016, *MNRAS*, 456, 3157
- Kun, M., Kiss, Z. T., & Balog, Z. 2008, *Handbook of Star Forming Regions, Volume I*, 4, 136
- Ladd, E. F., & Hodapp, K.-W. 1997, *ApJ*, 474, 749
- Landolt, A. U. 1992, *AJ*, 104, 340
- Larson, K. A., Whittet, D. C. B., & Hough, J. H. 1996, *ApJ*, 472, 755
- Launhardt, R., & Henning, T. 1997, *A&A*, 326, 329
- Lee, C. D., Eswaraiah, C., Chen, W. P., & Pandey, A. K. 2018, *AJ*, 156, 115

- Li, H.-B., Jiang, H., Fan, X., Gu, Q., & Zhang, Y. 2017, *Nature Astronomy*, 1, 0158
- Li, H.-b., & Houde, M. 2008, *ApJ*, 677, 1151
- Lynds, B. T. 1962, *ApJS*, 7, 1
- Maheswar, G., & Bhatt, H. C. 2006, *MNRAS*, 369, 1822
- Maheswar, G., Lee, C. W., Bhatt, H. C., Mallik, S. V., & Dib, S. 2010, *A&A*, 509, A44
- Maheswar, G., & Bhatt, H. C. 2006, *MNRAS*, 369, 1822
- Medhi, B. J., Maheswar, G., Pandey, J. C., Kumar, T. S., & Sagar, R. 2008, *MNRAS*, 388, 105
- McKee, C. F., & Ostriker, E. C. 2007, *ARA&A*, 45, 565
- Molinari, S., Swinyard, B., Bally, J., et al. 2010, *A&A*, 518, L100
- Moscadelli, L., Reid, M. J., Menten, K. M., et al. 2009, *ApJ*, 693, 406
- Mouschovias, T. C. 1976, *ApJ*, 207, 141
- Mouschovias, T. C. 1991, *ApJ*, 373, 169
- Mouschovias, T. C., & Ciolek, G. E. 1999, *NATO Advanced Science Institutes (ASI) Series C*, 540, 305
- Myers, P. C., & Benson, P. J. 1983, *ApJ*, 266, 309
- Myers, P. C., & Goodman, A. A. 1991, *ApJ*, 373, 509
- Nakano, T., & Nakamura, T. 1978, *PASJ*, 30, 671
- Neckel, T., Chini, R., Guesten, R., & Wink, J. E. 1985, *A&A*, 153, 253
- Neckel, T., & Chini, R. 1981, *A&AS*, 45, 451
- Neckel, T., & Staude, H. J. 1990, *A&A*, 231, 165
- Neha, S., Maheswar, G., Soam, A., & Lee, C. W. 2018, *MNRAS*, 476, 4442
- Olofsson, S., & Olofsson, G. 2010, *A&A*, 522, A84
- Ostriker, E. C., Stone, J. M., & Gammie, C. F. 2001, *ApJ*, 546, 980
- Pandey, A. K., Ogura, K., & Sekiguchi, K. 2000, *PASJ*, 52, 847
- Pandey, A. K., Upadhyay, K., Nakada, Y., & Ogura, K. 2003, *A&A*, 397, 191
- Pandey, A. K., Eswaraiah, C., Sharma, S., et al. 2013, *ApJ*, 764, 172
- Pandey, A. K., Samal, M. R., Chauhan, N., et al. 2013, *NewA*, 19, 1
- Peterson, D. E., & Clemens, D. P. 1998, *AJ*, 116, 881
- Planck Collaboration, Ade, P. A. R., Aghanim, N., et al. 2014, *A&A*, 571, A1
- Planck Collaboration, Ade, P. A. R., Aghanim, N., et al. 2016, *A&A*, 586, A138
- Poidevin, F., Bastien, P., & Matthews, B. C. 2010, *ApJ*, 716, 893
- Pudritz, R. E., Ouyed, R., Fendt, C., & Brandenburg, A. 2007, *Protostars and Planets V*, 277
- Puga, E., Marín-Franch, A., Najarro, F., et al. 2010, *A&A*, 517, A2
- Ramaprakash, A. N., Gupta, R., Sen, A. K., & Tandon, S. N. 1998, *A&AS*, 128, 369
- Rautela, B. S., Joshi, G. C., & Pandey, J. C. 2004, *Bulletin of the Astronomical Society of India*, 32, 159
- Reipurth, B. 1983, *A&A*, 117, 183
- Reipurth, B. 2008, *Handbook of Star Forming Regions, Volume II*, 5
- Richer, J. S., Shepherd, D. S., Cabrit, S., Bachiller, R., & Churchwell, E. 2000, *Protostars and Planets IV*, 867
- Rieke, G. H., & Lebofsky, M. J. 1985, *ApJ*, 288, 618
- Samal, M. R., Pandey, A. K., Ojha, D. K., et al. 2007, *ApJ*, 671, 555
- Santos, F. P., Roman-Lopes, A., & Franco, G. A. P. 2012, *ApJ*, 751, 138
- Santos, F. P., Busquet, G., Franco, G. A. P., Girart, J. M., & Zhang, Q. 2016, *ApJ*, 832, 186
- Sargent, A. I. 1977, *ApJ*, 218, 736
- Scappini, F., & Codella, C. 1996, *MNRAS*, 282, 587
- Schmidt, G. D., Elston, R., & Lupie, O. L. 1992, *AJ*, 104, 1563
- Sen, A. K., & Tandon, S. N. 1994, *Proc. SPIE*, 2198, 264
- Serkowski, K., Mathewson, D. S., & Ford, V. L. 1975, *ApJ*, 196, 261
- Sharma, S., Pandey, A. K., Ojha, D. K., et al. 2017, *MNRAS*, 467, 2943
- Sofue, Y., & Kataoka, J. 2016, *PASJ*, 68, L8
- Soler, J. D., Alves, F., Boulanger, F., et al. 2016, *A&A*, 596, A93
- Sugitani, K., Nakamura, F., Tamura, M., et al. 2010, *ApJ*, 716, 299
- Shu, F. H. 1977, *ApJ*, 214, 488
- Shu, F. H., Lizano, S., & Adams, F. C. 1987, *Star Forming Regions*, 115, 417
- Stecklum, B., Melnikov, S. Y., & Meusinger, H. 2007, *A&A*, 463, 621
- Su, Y., Sun, Y., Li, C., et al. 2016, *ApJ*, 828, 59
- Su, Y., Zhou, X., Yang, J., et al. 2017, *ApJ*, 836, 211
- Torii, K., Hasegawa, K., Hattori, Y., et al. 2015, *ApJ*, 806, 7
- Taylor, A. R., Gibson, S. J., Peracaula, M., et al. 2003, *AJ*, 125, 3145
- Ungerechts, H., Umbanhowar, P., & Thaddeus, P. 2000, *ApJ*, 537, 221
- Vallée, J. P. 2002, *AJ*, 123, 382
- Valencic, L. A., & Smith, R. K. 2015, *ApJ*, 809, 66
- Vrba, F. J., Luginbuhl, C. B., Strom, S. E., Strom, K. M., & Heyer, M. H. 1986, *AJ*, 92, 633
- Wang, J.-W., Lai, S.-P., Eswaraiah, C., et al. 2017, *ApJ*, 849, 157
- Ward-Thompson, D., Kirk, J. M., Crutcher, R. M., et al. 2000, *ApJL*, 537, L135
- Welty, D. E., & Fowler, J. R. 1992, *ApJ*, 393, 193
- Whitney, B. A., Robitaille, T. P., Indebetouw, R., et al. 2005, *Massive Star Birth: A Crossroads of Astrophysics*, 227, 206
- Whittet, D. C. B. 2005, *Astronomical Polarimetry: Current Status and Future Directions*, 343, 321
- Whittet, D. C. B., Hough, J. H., Lazarian, A., & Hoang, T. 2008, *ApJ*, 674, 304

Whittet, D. C. B. 2003, *Dust in the galactic environment*, 2nd ed. by D.C.B. Whittet. Bristol: Institute of Physics (IOP) Publishing, 2003 Series in Astronomy and Astrophysics, ISBN 0750306246.

Yonekura, Y., Dobashi, K., Mizuno, A., Ogawa, H., & Fukui, Y. 1997, *ApJS*, 110, 21

Yu, Z.-Y., Nagahama, T., & Fukui, Y. 1996, *ApJ*, 471, 867

Zinn, J. C., Pinsonneault, M. H., Huber, D., & Stello, D. 2018, [arXiv:1805.02650](https://arxiv.org/abs/1805.02650)

## APPENDIX

A. COLOR-COLOR DIAGRAMS AND ESTIMATION OF TOTAL-TO-SELECTIVE EXTINCTION ( $R_V$ )

Figure 16 shows the color-color diagrams of the 111 FG stars (with distances  $< 830$  pc) and 375 BG stars (distances between 830 pc – 2.65 kpc) depicted using blue and red filled circles, respectively. There exist 27 and 16 M-type stars among the FG and BG stars, respectively, and are shown with overlapping squares. These M-type stars are identified based on a comparison of their  $(B-V)$  vs  $(V-I)$  colors with the intrinsic locus of M-type dwarfs (Peterson et al 1998) shown with a curve in the top left panel of Figure 16. We have excluded M-type stars from the further analysis because they would effect the true reddening law of the cloud by occupying the location of reddened background stars. The remaining 92 FG stars and 351 BG stars with photometry (hereafter group I) were used to perform the weighted linear fits and the resultant slopes are given in Table 6. Similarly, shown in Figure 17, we also estimate the slopes based on the weighted linear fits to the color-color combinations of 30 FG and 57 BG stars with photometry plus polarimetry (hereafter group II). The fitted slopes along with their uncertainties are given in Table 6. In the group I, M-type stars seem to have more contamination on the reddened BG stars (Figure 16), in contrast this is not pronounced in group II (Figure 17).

To estimate the value of  $R_V$  for LDN 1225, we use the following relation of the form (see Neckel et al 1981)

$$R_V = \frac{m}{m_{normal}} R_{normal}, \quad (A1)$$

where  $m$  and  $m_{normal}$  are the slopes of the two-color combinations, respectively, for the FG or BG stars and unreddened main-sequence stars following the normal extinction law (taken from the stellar models by Bertelli et al 1994, and also see Table 3 of Pandey et al 2003).  $R_{normal}$  corresponds to normal extinction law and is considered to be 3.1. Using the equation (A1) and the fitted slopes (cf. columns 3 and 5 of Table 6), we estimate  $R_V$  values along with their uncertainties for the FG and BG stars of the two groups and are given in columns 4 and 6 of Table 6. The weighted mean  $R_V$  values are  $3.10 \pm 0.01$  (standard deviation = 0.14) and  $3.36 \pm 0.01$  (standard deviation = 0.14), respectively, for FG and BG stars of the group I. Similarly, the weighted mean  $R_V$  values are  $2.87 \pm 0.01$  (standard deviation = 0.12) and  $3.41 \pm 0.01$  (standard deviation = 0.15), respectively, for the FG and BG stars of the group II. Discussion based on the derived  $R_V$  values is given in Section 4.9.

B. ESTIMATION OF VISUAL EXTINCTION ( $A_V$ )

Figure 18 shows the NIR color-color ( $(J-H)$  versus  $(H-K_s)$ ) diagram of 113 stars having polarization data. NIR photometric data of these stars were extracted from Two Micron All Sky Survey (2MASS) point source catalog (Cutri et al 2003). All the sources have uncertainties less than 0.1 mag corresponds to signal-to-noise ratio (SNR)  $> 10$  and with photometric quality flag of “AAA” in  $JHK_s$ -bands. NIR extinction method estimates  $A_V$  value of a star by dereddening its observed colors ( $(J-H)$  and  $(H-K_s)$ ) to match with its intrinsic colors ( $(J-H)_0$  and  $(H-K_s)_0$ ) by using the following relations (cf. Maheswar et al 2010):

$$(J-H)_0 = (J-H) - 0.107 \times A_V, \quad (B2)$$

$$(H-K_s)_0 = (H-K_s) - 0.063 \times A_V \quad (B3)$$

These relations utilize the extinction law of Rieke et al (1985). In this method, various  $A_V$  values having the interval of 0.01 mag were used for dereddening the observed colors, and these sets of dereddened colors were matched to the intrinsic colors as illustrated in the Figure 18 using a blue arrow. The  $A_V$  value at which the dereddened colors matched to the intrinsic colors, giving a minimum Chi-square value, yields a best  $A_V$  of a star. NIR extinction method (Maheswar et al 2010) has been employed only to the 57 stars having  $(J-K_s) \leq 0.75$  mag as shown with filled circles. The derived maximum value of extinction through this method comes out to be  $A_V \approx 4$  mag. The criterion  $(J-K_s) \leq 0.75$  excludes the unreddened/reddened M-type stars, giants, and classical T-Tauri stars. We also exclude stars distributed left side to the MS locus. All the excluded 56 stars are denoted with gray filled circles. The uncertainty in  $A_V$  values are estimated by using equation (10) of Maheswar et al (2010).

Estimated  $A_V$  values along with uncertainties for 57 stars are listed in Table 7. This table also lists the IDs, coordinates, NIR colors, polarization values. Further analysis uses only 32 stars and satisfying the criteria  $A_V/\sigma_{A_V} \geq 2$ . The derived  $2\sigma$   $A_V$  values range from 0.9 mag to 3.3 mag with mean of  $2.0 \pm 0.6$  mag<sup>8</sup>. Based on the  $A_V$  and polarization values, polarization efficiency of the dust grains of LDN 1225 is discussed in Section 4.10.

<sup>8</sup> The corresponding mean column density is  $N_{H_2} = (2.2 \pm 0.2) \times 10^{21} \text{ cm}^{-2}$  (using the relations  $N_H = 2N_{H_2}$  and  $N_H = (2.21 \pm 0.09) \times 10^{21} A_V \text{ mag}^{-1} \text{ cm}^{-2}$ ; see Güver & Özel 2009; Valencic & Smith 2015). This value, within the error, is consistent with the column density,  $(3.4 \pm 1.3) \times 10^{21} \text{ cm}^{-2}$ , derived using the  $^{12}\text{CO}$  integrated emission of LDN 1225 (cf., Section 3.7).



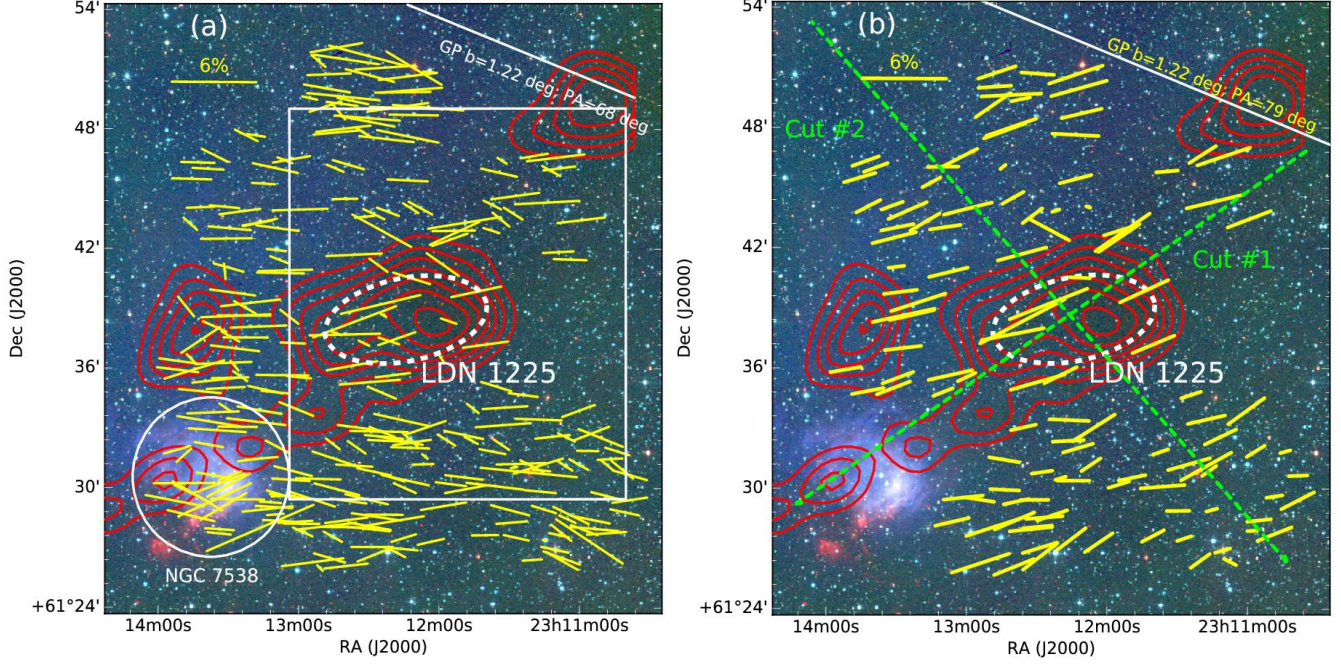


**Figure 1.** B-field orientation towards LDN 1225 before and after exclusion of unwanted stars (such as FG and BG-NGC 7538 stars, stars around NGC 7538, NIR excess sources) and correction of ISP from the polarizations of BG stars. (a) Polarization vector map of the region containing LDN 1225, using  $P_R$  and  $\theta_R$  values of all 280 stars. Background is the color-composite of 2MASS  $K_s$ - (red), DSS I- (green) and DSS R-band (blue) images. Red contours represent the  $^{12}\text{CO}$  total integrated intensity map, drawn at 3, 6, 9, 12, 15, 18, 21, and 24  $\text{K km s}^{-1}$ . Location of the dark globule LDN 1225 and the star-forming region NGC 7538 (with a circle of  $8'$  diameter) are shown and labeled. White dashed ellipse denotes the extent (major axis =  $8.4'$  diameter, minor axis =  $4.2'$  diameter, and position angle =  $102^\circ$ ) of LDN 1225 based on the CO data (see Figure 8). Reference vector with  $P_R = 6\%$  and  $\theta_R = 90^\circ$  is shown. Galactic plane making a position angle (PA) of  $68^\circ$  towards LDN 1225 is shown with a white line. White box with the dimensions of  $\sim 17' \times 20'$  marks the region around LDN 1225 selected for optical photometry in  $BVRI$ -bands. (b) Same as (a) but depicts the B-field map of LDN 1225 cloud using the polarization measurements ( $P_C$  and  $\theta_C$ ) of 118 BG stars having accounted for interstellar polarization (see section 3.5). Two PV cuts are shown and labeled. Cut 1 is parallel (with position angle of  $\sim 124^\circ$ ) and cut 2 is perpendicular (with position angle  $\sim 222^\circ$ ) to the elongation of the LDN 1225.

**Table 1.**  $R_c$ -band measurements of polarized standard stars.

Date	$P_{R_c}(\%)$	$\theta_{R_c}(^\circ)$	$P_{R_c}(\%)$	$\theta_{R_c}(^\circ)$
	Our work		Schmidt et al (1992)	
Polarized standard HD 19820				
02 Nov 2013	$4.6 \pm 0.1$	$114.6 \pm 0.6$	$4.53 \pm 0.03$	$114.5 \pm 0.2$
12 Nov 2010	$4.6 \pm 0.1$	$114.5 \pm 0.4$	$4.53 \pm 0.03$	$114.5 \pm 0.2$
13 Dec 2010	$4.6 \pm 0.1$	$114.2 \pm 0.4$	$4.53 \pm 0.03$	$114.5 \pm 0.2$
Polarized standard HD 204827				
13 Nov 2010	$4.9 \pm 0.1$	$59.2 \pm 0.5$	$4.89 \pm 0.03$	$59.1 \pm 0.2$
Polarized standard BD+59° 389				
14 Dec 2010	$6.5 \pm 0.1$	$97.7 \pm 0.4$	$6.43 \pm 0.02$	$98.1 \pm 0.1$
01 Nov 2013	$6.3 \pm 0.1$	$98.0 \pm 0.4$	$6.43 \pm 0.02$	$98.1 \pm 0.1$
Unpolarized standard HD 21447				
14 Dec 2010	$0.05 \pm 0.1$	$156 \pm 56$	$0.05 \pm 0.02^\dagger$	$171.5^\dagger$

NOTE— $^\dagger$  V-band results from Schmidt et al (1992)

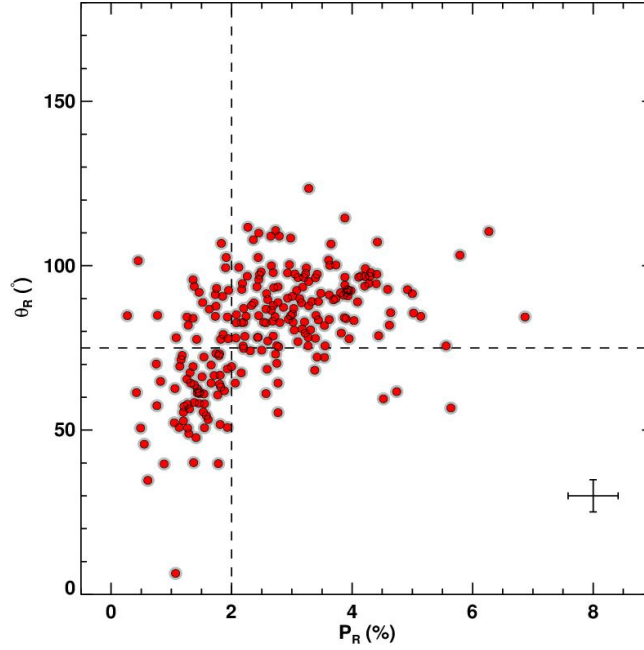


**Figure 2.** Polarization ( $P_R$ ) versus polarization angle ( $\theta_R$ ) of 238 stars located towards LDN 1225 using filled red circles. Two populations of stars with different values of  $P_R$  and  $\theta_R$  are evident and are separated by dashed lines drawn at  $P_R = 2\%$  and  $\theta_R = 75^\circ$ . Typical error is shown at the bottom-right side of the plot.

**Table 2.**  $R_C$ -band polarization data of 280 stars along with their photometric data from 2MASS catalog, distances from GAIA DR2, and stellar classification based on our analyses.

ID	R.A (J2000)	Dec (J2000)	$P_R$	$\theta_R$	$J$	$H$	$K_s$	distance	classification
(1)	(h:m:s)	(deg : ' : '')	(%)	(deg)	(mag)	(mag)	(mag)	(pc)	(10)
1	23:10:38.082	61:30:40.208	$2.5 \pm 0.9$	$74 \pm 10$	$14.22 \pm 0.04$	$13.70 \pm 0.04$	$13.51 \pm 0.04$	$1098 \pm 53$	BG
2	23:10:38.271	61:29:25.339	$2.5 \pm 0.4$	$98 \pm 5$	$11.83 \pm 0.03$	$11.02 \pm 0.03$	$10.84 \pm 0.02$	$2380 \pm 152$	BG
3	23:10:40.539	61:28:48.878	$2.1 \pm 0.3$	$78 \pm 5$	$12.73 \pm 0.03$	$12.40 \pm 0.03$	$12.29 \pm 0.02$	$669 \pm 10$	FG
4	23:10:41.364	61:30:57.006	$1.9 \pm 0.2$	$51 \pm 3$	$12.06 \pm 0.03$	$11.67 \pm 0.03$	$11.59 \pm 0.02$	$460 \pm 4$	FG
5	23:10:43.502	61:31:52.251	$1.8 \pm 0.5$	$73 \pm 8$	$13.47 \pm 0.03$	$13.09 \pm 0.03$	$12.97 \pm 0.03$	$843 \pm 20$	BG
6	23:10:46.677	61:31:29.056	$1.8 \pm 0.2$	$93 \pm 3$	$10.84 \pm 0.03$	$10.01 \pm 0.03$	$9.78 \pm 0.02$	$2668 \pm 159$	BG-NGC7538
7	23:10:47.868	61:31:10.794	$1.1 \pm 0.3$	$51 \pm 7$	$12.90 \pm 0.03$	$12.41 \pm 0.03$	$12.35 \pm 0.03$	$517 \pm 6$	FG
8	23:10:48.248	61:29:38.274	$2.2 \pm 0.5$	$76 \pm 6$	$13.65 \pm 0.04$	$13.15 \pm 0.05$	$13.06 \pm 0.04$	$2078 \pm 145$	BG
9	23:10:48.262	61:27:45.871	$2.8 \pm 0.5$	$94 \pm 5$	$13.40 \pm 0.03$	$13.07 \pm 0.04$	$12.84 \pm 0.03$	$1061 \pm 32$	BG
10	23:10:50.616	61:32:33.244	$3.4 \pm 0.4$	$68 \pm 3$	$10.77 \pm 0.03$	$9.43 \pm 0.03$	$9.02 \pm 0.02$	—	—
11	23:10:53.417	61:27:59.151	$3.4 \pm 0.3$	$85 \pm 3$	$10.60 \pm 0.03$	$9.31 \pm 0.03$	$8.96 \pm 0.02$	$3206 \pm 601$	BG-NGC7538
12	23:10:54.662	61:32:45.974	$2.7 \pm 0.7$	$111 \pm 7$	$14.23 \pm 0.03$	$13.71 \pm 0.03$	$13.46 \pm 0.04$	$3812 \pm 615$	BG-NGC7538
13	23:10:54.854	61:28:26.958	$2.7 \pm 0.5$	$79 \pm 5$	$13.57 \pm 0.02$	$13.24 \pm 0.03$	$13.13 \pm 0.02$	$1497 \pm 67$	BG
14	23:10:55.633	61:27:21.798	$5.6 \pm 0.4$	$57 \pm 2$	$12.10 \pm 0.03$	$11.54 \pm 0.03$	$11.29 \pm 0.02$	$5519 \pm 981$	BG-NGC7538
15	23:10:56.201	61:31:54.080	$1.5 \pm 0.5$	$89 \pm 10$	$14.15 \pm 0.03$	$13.91 \pm 0.05$	$13.72 \pm 0.05$	$2141 \pm 179$	BG

NOTE—A portion of the table is given here, and the entire table will be available in the online version of the paper.

NOTE—†: The stars distributed within  $8'$  area (circle in Figure 1(a)) containing the star-forming region NGC 7538.

NOTE—‡: The stars with NIR excess emission.

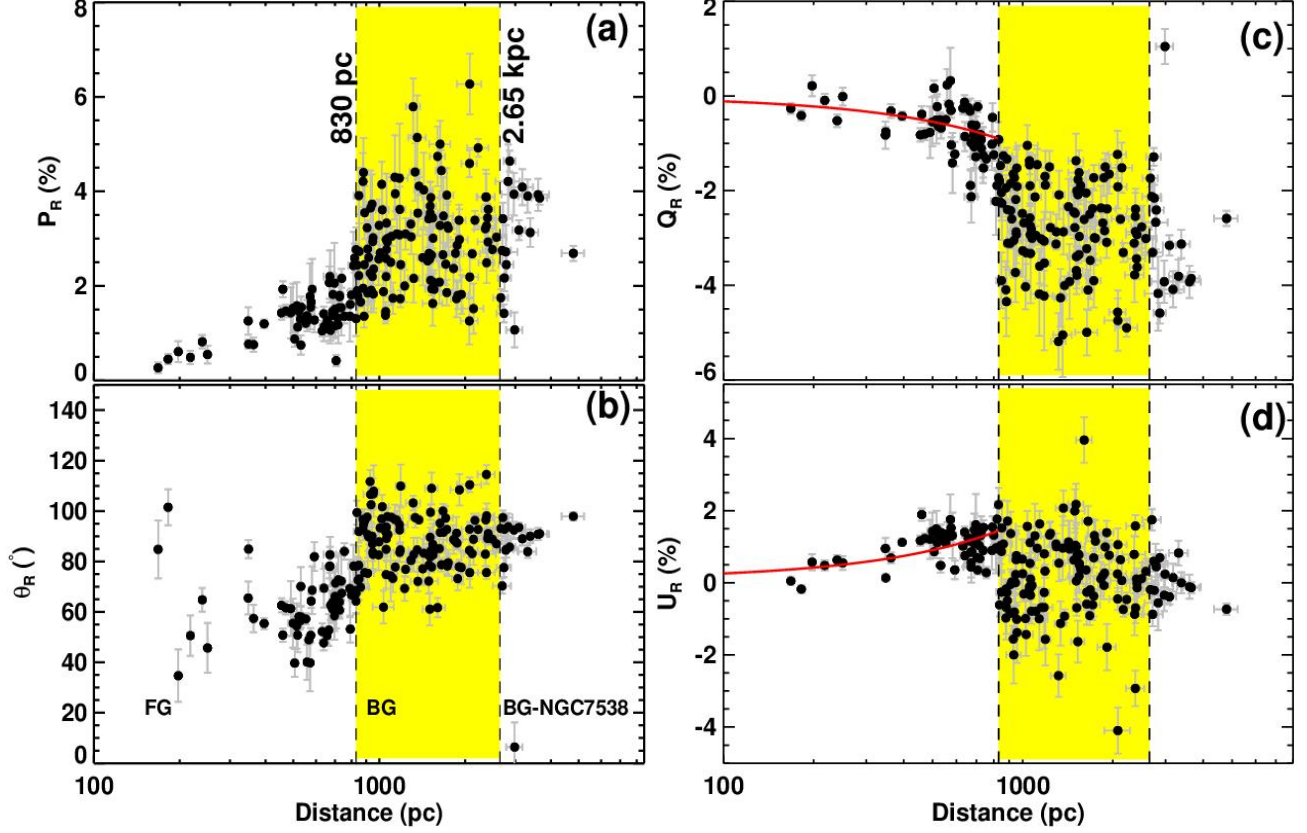


**Figure 3.** Distance versus  $P_R$  (a) and  $\theta_R$  (b) of 197 stars satisfying the criterion  $\omega/\sigma_\omega \geq 10$ . Distance versus  $Q_R$  (c) and  $U_R$  (d) of the same stars plotted in panels (a) and (b). Abrupt increase in  $P_R$  and  $\theta_R$  values, and abrupt change in  $Q_R$ , and  $U_R$  values are witnessed at a distance of 830 pc. Weighted linear fits made to the  $Q_R$  and  $U_R$  versus distance values, using 61 stars with distances  $< 830$  pc, are shown with red thick lines (see text for more details).

**Table 3.** Photometric data of 689 stars with their photometric uncertainties less than 0.1 mag.

ID	R.A (J2000)	Dec (J2000)	V	(B-V)	(V-R)	(V-I)	J	H	$K_s$
(1)	(h:m:s)	( $^{\circ}$ : ' : ")	(mag)	(mag)	(mag)	(mag)	(mag)	(mag)	(mag)
1	23:10:41.320	61:39:19.299	18.349 $\pm$ 0.011	1.382 $\pm$ 0.028	0.871 $\pm$ 0.008	1.693 $\pm$ 0.044	15.47 $\pm$ 0.05	14.89 $\pm$ 0.07	14.66 $\pm$ 0.09
2	23:10:41.723	61:36:52.675	16.572 $\pm$ 0.004	1.291 $\pm$ 0.008	0.747 $\pm$ 0.003	1.525 $\pm$ 0.010	14.22 $\pm$ 0.03	13.68 $\pm$ 0.04	13.56 $\pm$ 0.05
3	23:10:41.759	61:34:45.177	16.364 $\pm$ 0.010	1.121 $\pm$ 0.016	0.686 $\pm$ 0.009	1.347 $\pm$ 0.009	14.15 $\pm$ 0.04	13.64 $\pm$ 0.04	13.56 $\pm$ 0.09
4	23:10:42.002	61:36:39.916	17.455 $\pm$ 0.006	1.097 $\pm$ 0.012	0.710 $\pm$ 0.005	1.497 $\pm$ 0.022	15.14 $\pm$ 0.04	14.83 $\pm$ 0.06	14.57 $\pm$ 0.08
5	23:10:42.061	61:37:36.948	18.338 $\pm$ 0.010	1.284 $\pm$ 0.026	0.875 $\pm$ 0.009	1.861 $\pm$ 0.037	15.48 $\pm$ 0.06	14.71 $\pm$ 0.05	14.73 $\pm$ 0.09
6	23:10:42.204	61:37:43.968	17.588 $\pm$ 0.005	1.053 $\pm$ 0.012	0.722 $\pm$ 0.006	1.558 $\pm$ 0.022	15.15 $\pm$ 0.07	14.62 $\pm$ 0.07	14.44 $\pm$ 0.08
7	23:10:42.624	61:42:52.848	16.808 $\pm$ 0.004	1.108 $\pm$ 0.011	0.782 $\pm$ 0.005	1.568 $\pm$ 0.003	14.30 $\pm$ 0.03	13.80 $\pm$ 0.04	13.64 $\pm$ 0.04
8	23:10:42.651	61:36:19.713	16.675 $\pm$ 0.004	1.013 $\pm$ 0.007	0.669 $\pm$ 0.004	1.401 $\pm$ 0.011	14.53 $\pm$ 0.03	14.01 $\pm$ 0.04	13.93 $\pm$ 0.04
9	23:10:42.981	61:43:32.314	16.859 $\pm$ 0.004	1.098 $\pm$ 0.011	0.764 $\pm$ 0.004	1.524 $\pm$ 0.003	14.48 $\pm$ 0.04	13.92 $\pm$ 0.05	13.77 $\pm$ 0.04
10	23:10:43.080	61:47:15.529	18.162 $\pm$ 0.006	1.639 $\pm$ 0.040	1.141 $\pm$ 0.005	2.116 $\pm$ 0.006	14.76 $\pm$ 0.04	14.03 $\pm$ 0.05	13.78 $\pm$ 0.05
11	23:10:43.417	61:30:41.061	18.966 $\pm$ 0.018	1.867 $\pm$ 0.073	1.137 $\pm$ 0.012	2.391 $\pm$ 0.046	15.52 $\pm$ 0.06	14.56 $\pm$ 0.05	14.52 $\pm$ 0.08
12(5)	23:10:43.502	61:31:52.251	15.229 $\pm$ 0.006	0.981 $\pm$ 0.003	0.534 $\pm$ 0.002	1.090 $\pm$ 0.006	13.47 $\pm$ 0.03	13.09 $\pm$ 0.03	12.97 $\pm$ 0.03

NOTE—A portion of the table is given here, and the entire table will be available in the online version of the paper.

NOTE—In column 1, star IDs mentioned in parentheses are the stars having polarization data (Table 2)



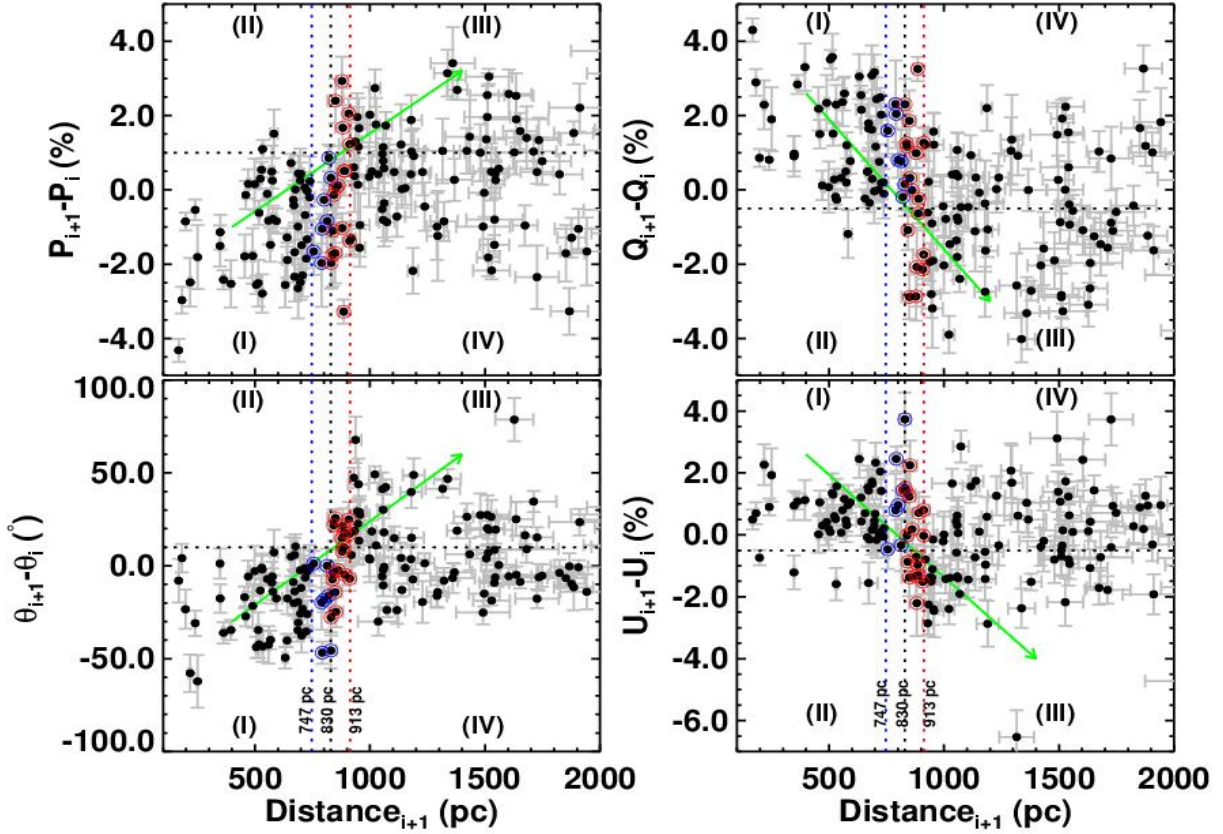


**Figure 4.** Differential polarization ( $P_{i+1} - P_i$ ), polarization angles ( $\theta_{i+1} - \theta_i$ ), and Stokes parameters ( $Q_{i+1} - Q_i$  and  $U_{i+1} - U_i$ ) versus distance ( $Distance_{i+1}$ ) parameters for the stars used in Figure 3. We used the data up to 2 kpc and distance in linear scale. Black vertical (at 830 pc) and horizontal dotted lines in each panel separates the entire data samples into four regions. Region II is devoid of the data (at most four stars in panel of  $U_{i+1} - U_i$  vs  $Distance_{i+1}$ ) in comparison to those in other three regions (I, III, and IV). In all the panels, region I is dominated by the FG stars, while the regions III and IV with BG stars. Blue and red dotted vertical lines are drawn, respectively, at 747 pc and 913 pc corresponding to the lower and upper limits of the ascertained distance 830 pc with an uncertainty of 83 pc for LDN 1225. Blue circles represent the stars distributed between  $747 \text{ pc} < Distance_{i+1} < 830 \text{ pc}$ , while the red circles with  $830 \text{ pc} < Distance_{i+1} < 913 \text{ pc}$ . Green arrow marks a clear transition of the differential parameters from negative to positive (or vice versa) at the distance of 830 pc.

**Table 4.** Weighted mean polarization measurements of FG and BG stars (ISP corrected) of various fields of CepOB3. Also given are the central coordinates and number of stars in each field, the passband, and the instrument or source used for the data.

Field/HD number	RA (J2000)	Dec (J2000)	weighted mean $P$	weighted mean $\theta$	pass-band	No. of stars	instrument (or) source
(1)	(h:m:s)	( $^{\circ}$ : ' : ")	(%)	( $^{\circ}$ )	(6)	(7)	(8)
FG stars with $d < 830 \text{ pc}$							
1	22:56:53.332	62:09:58.572	$0.54 \pm 0.14$	$63 \pm 7$	R	4	AIMPOL
2	22:56:33.530	62:04:54.912	$2.20 \pm 0.10$	$73 \pm 1$	R	5	..
3	22:56:07.713	61:58:02.352	$1.19 \pm 0.08$	$109 \pm 2$	R	5	..
4	22:57:41.210	62:41:51.792	$1.29 \pm 0.13$	$69 \pm 3$	R	2	IMPOL
5	22:58:16.408	62:43:25.176	–	–	R	0	..
6	22:57:02.560	62:39:01.188	$0.61 \pm 0.03$	$68 \pm 1$	R	4	..
7	22:56:50.930	62:34:53.292	$1.31 \pm 0.06$	$76 \pm 1$	R	3	..
8	22:56:51.355	62:31:18.084	$1.41 \pm 0.03$	$83 \pm 1$	R	4	..
9	22:58:19.392	62:38:45.744	$0.11 \pm 0.06$	$75 \pm 14$	R	1	..
10	22:57:34.209	62:35:53.484	$1.00 \pm 0.07$	$163 \pm 2$	R	3	..

NOTE—RA and Dec (except those of the stars from Heiles (2000)) are the central coordinates of the observed fields.

NOTE—A portion of the table is given here, and the entire table will be available in the online version of the paper.



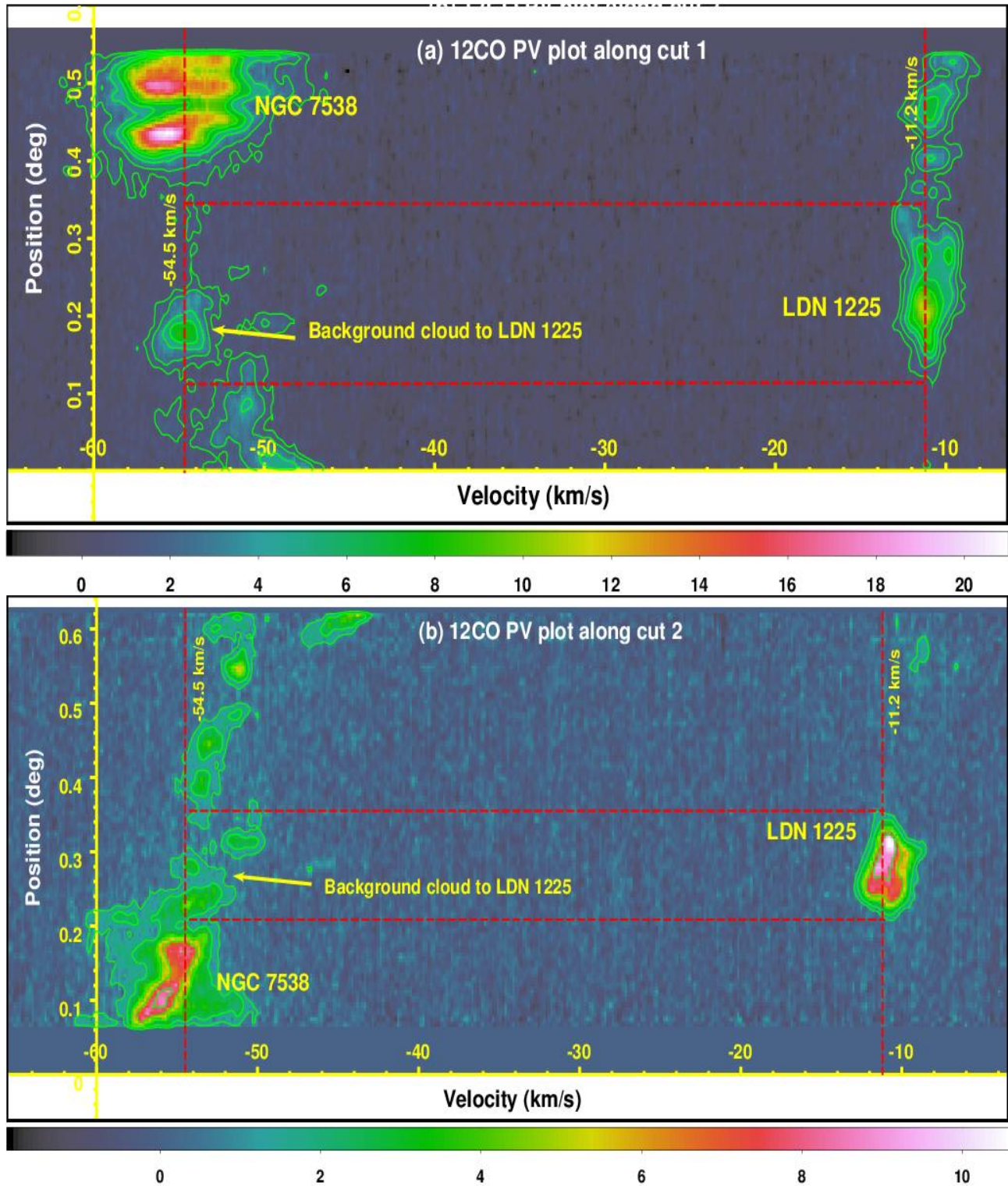


**Figure 5.**  $^{12}\text{CO}$  position-velocity (PV) plots along the two cuts shown in Figure 1(b). (a) PV plot for cut 1 (parallel to the elongation of LDN 1225). (b) Same as (b) but along the cut 2 (perpendicular to the elongation of LDN 1225). Green contours, correspond to the  $^{12}\text{CO}$  intensity, are drawn at 1, 2, 4, 6, and 8 K. Vertical dashed lines drawn at  $-11.2 \text{ km s}^{-1}$  and  $-54.52 \text{ km s}^{-1}$ , respectively, corresponds to LDN 1225 and its background cloud located at similar velocity of NGC 7538. Horizontal dashed lines depict the spatial extent of LDN 1225 emission for a given cut.

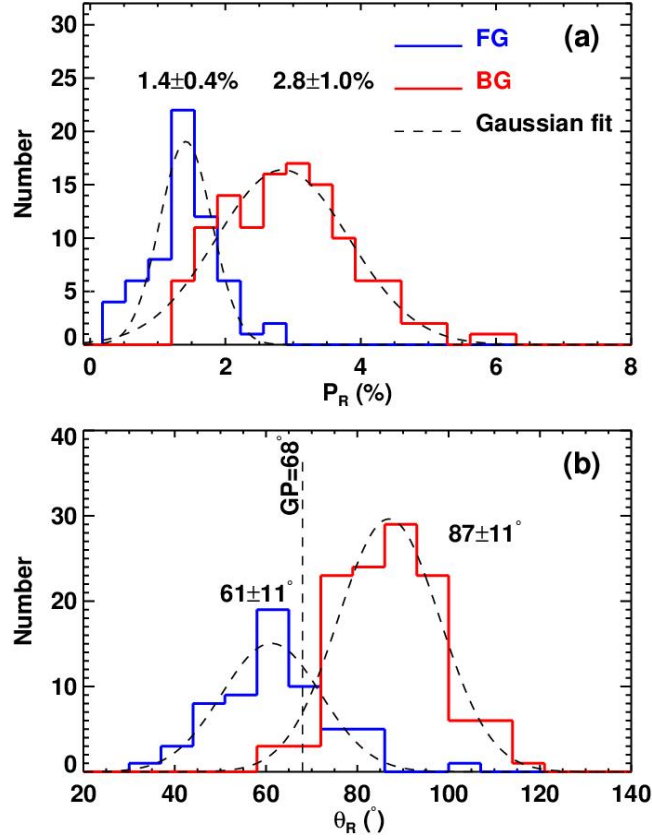


**Figure 6.** (a) Number distribution of  $P_R$  of the FG and BG stars, and the corresponding Gaussian fits are shown with dotted lines. Fitted mean and standard deviations are  $1.4 \pm 0.4\%$  and  $2.8 \pm 1.0\%$ . (b) Same as panel (a) but for  $\theta_R$  distributions of FG and BG stars. Gaussian fitted mean and standard deviations are  $61 \pm 11^\circ$  and  $87 \pm 11^\circ$ . The position angle of the Galactic parallel (GP =  $68^\circ$ ) is drawn.

**Table 5.** Spatial extents and position angles of LDN 1225 based on the CASA 2D Gaussian function fitting to the moment 0 maps of  $^{12}\text{CO}$ ,  $^{13}\text{CO}$ , and  $\text{C}^{18}\text{O}$

Line	R.A (J2000) (h:m:s)	Dec (J2000) ( $^\circ$ : $'$ : $''$ )	$FWHM_{major}$ (arcmin)	$FWHM_{minor}$ (arcmin)	$\theta_{cloud}$ ( $^\circ$ )	$\Delta_\theta =  \theta_{cloud} - \theta_C $ ( $^\circ$ )
(1)	(2)	(3)	(4)	(5)	(6)	(7)
$^{12}\text{CO}$	23:12:16.62	61:38:24.27	$8.6 \pm 0.2$	$4.4 \pm 0.1$	$102 \pm 1$	$4 \pm 11$
$^{13}\text{CO}$	23:12:01.11	61:39:13.50	$4.4 \pm 0.1$	$3.1 \pm 0.1$	$52 \pm 3$	$54 \pm 11$
$\text{C}^{18}\text{O}$	23:11:55.60	61:39:15.00	$1.8 \pm 0.1$	$1.3 \pm 0.1$	$54 \pm 8$	$52 \pm 14$

NOTE— $\theta_C = 106 \pm 11^\circ$ , the mean B-field orientation in LDN 1225 after foreground (interstellar) polarization correction (cf. Section 3.5).

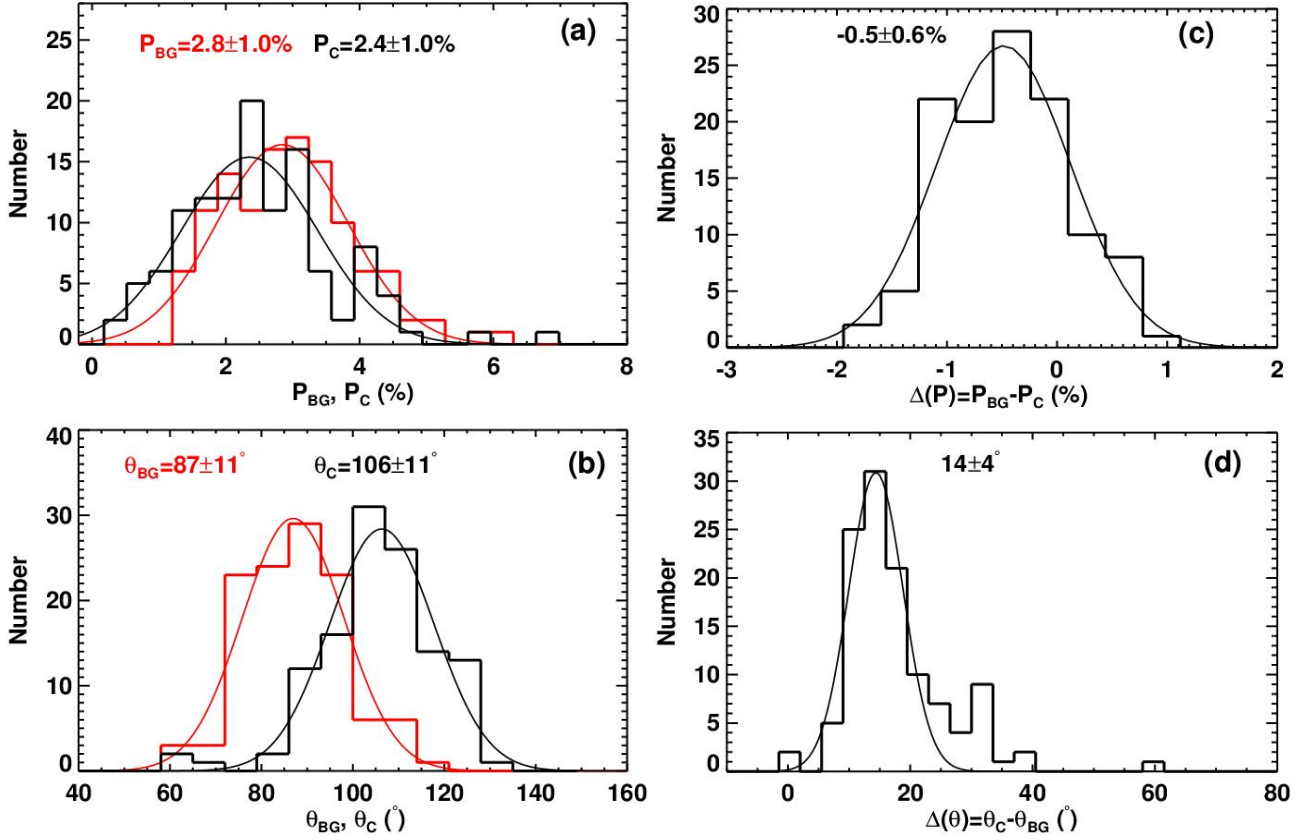


**Figure 7.** (a) Number distributions of  $P_{BG}$  and  $P_C$  of the BG stars before (red histograms) and after (black histograms) ISP correction. (b) Same as (b) but for  $\theta_{BG}$  and  $\theta_C$ . (c) and (d) Distributions of  $\Delta(P) = P_{BG} - P_C$  and  $\Delta(\theta) = \theta_C - \theta_{BG}$ , respectively. Gaussian fits and the resultant means and dispersions are shown in each panel.

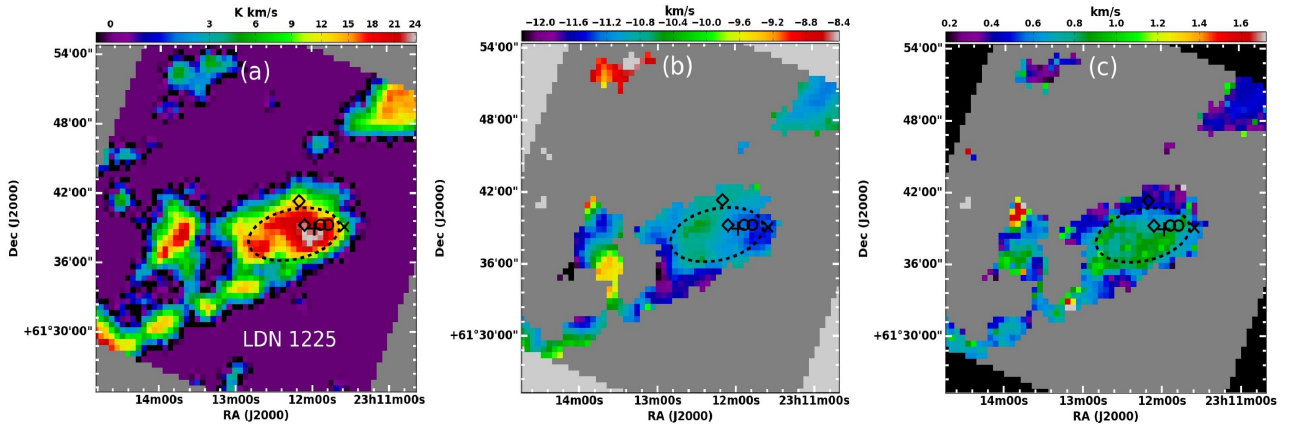


**Figure 8.**  $^{12}\text{CO}$  (1 – 0) moment maps of the  $30' \times 30'$  area containing LDN 1225 using the data from PMO as a part of the MWISP project. (a) CO total integrated intensity map (moment 0) of the region containing LDN 1225. (b) CO mean velocity map (moment 1). (c) CO velocity dispersion map (moment 2). These maps were made using the velocity channels ranging from  $\sim -13 \text{ km s}^{-1}$  to  $\sim -3 \text{ km s}^{-1}$  and having the brightness temperature above 3 times of the rms noise. Extent of the LDN 1225 is shown with a dashed ellipse with major and minor axes lengths of  $8.6'$  and  $4.3'$ , and with PA of  $102^\circ$ . Color bar in each panel corresponds to the respective map units. Cloud center of LDN 1225 is denoted with a plus symbol in all the panels. Location of IRAS 23094+6122 source is shown with a cross symbol. Circles and diamonds correspond to the *Herschel*/PACS  $70 \mu\text{m}$  and MIR sources, respectively. Within the area of LDN 1225, the distributions of gas velocity (panel b) as well as the gas dispersion (panel c) are found to be uniform.



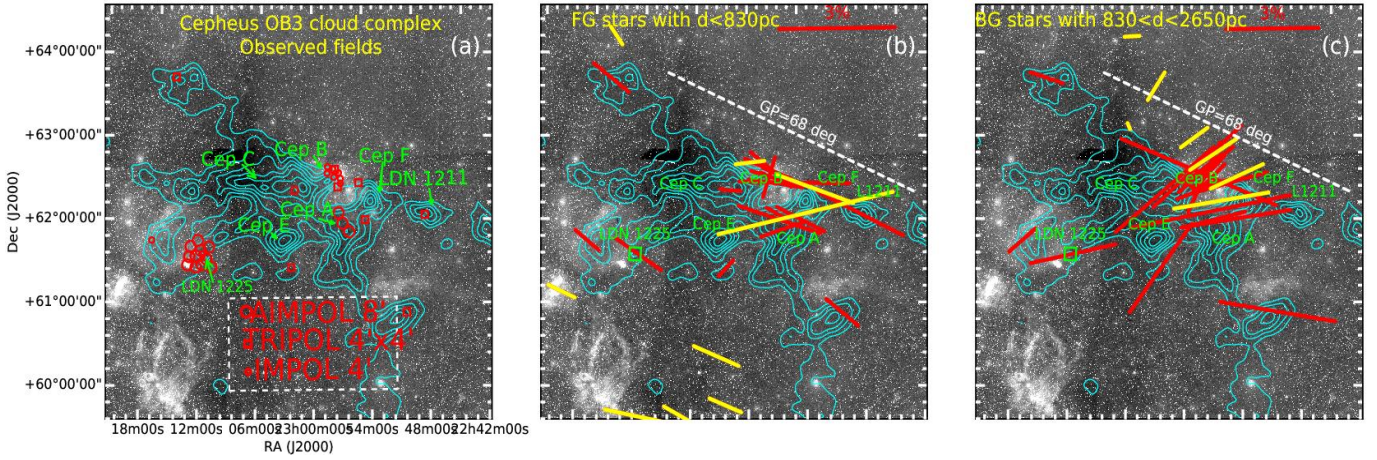


**Figure 9.** (a) Polarization measurements of several fields to infer the B-field orientation towards CepOB3. Observed fields with optical polarimeters AIMPOL, TRIPOL, and IMPOL, are shown and depicted. (b) B-field orientation in the foreground medium of CepOB3 using the weighted mean polarizations of stars with  $d < 830$  pc. (c) Same as (b) but corresponds to the B-field map of CepOB3 using the polarizations of BG stars with  $830 \text{ pc} < d < 2.65 \text{ kpc}$  and corrected for ISP contribution. Locations of the clumps and globules are shown. Note here that in case of a field having more than two stars, their weighted means are plotted; otherwise their single measurements are shown. Similarly, we also plotted FG and BG stars (ISP corrected) polarization with Heiles (2000) data using yellow vectors. In panels (a) and (b), the orientation of Galactic plane with a position angle of  $68^\circ$  and a reference vector with  $3\%$  and  $90^\circ$  are shown. In all the panels the background is the  $5^\circ \times 5^\circ$  DSS R-band image and the cyan contours correspond to the extinction ( $A_V$ ) map drawn from 2.5 to 6.5 mag with an interval of 0.5 mag (Dobashi et al 2005).

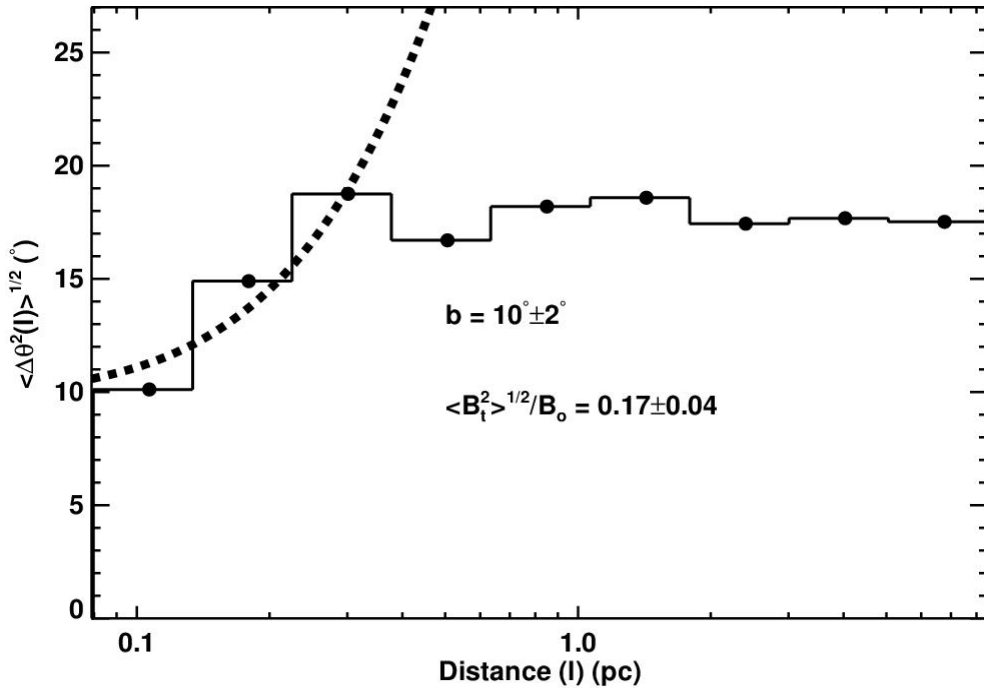


**Figure 10.** Plot shows square root of the second-order structure function (or angular dispersion function (ADF)),  $\langle \Delta(\theta^2(l)) \rangle^{1/2}$  (degree) versus the distance ( $l$ ) in pc. For this we have used the  $\theta_C$  of 118 BG stars. The filled circles are the ADF values in each bin (in log scale). The error bars are similar to the size of the symbols. The turbulent contribution to the total angular dispersion function is estimated by the intercept ( $b$ ) of the fit to the data at distance ( $l$ ) = 0. The measurements errors were corrected before fitting the function to the data. The thick dotted line corresponds to the best fit to the data for the distance less than 0.5 pc.





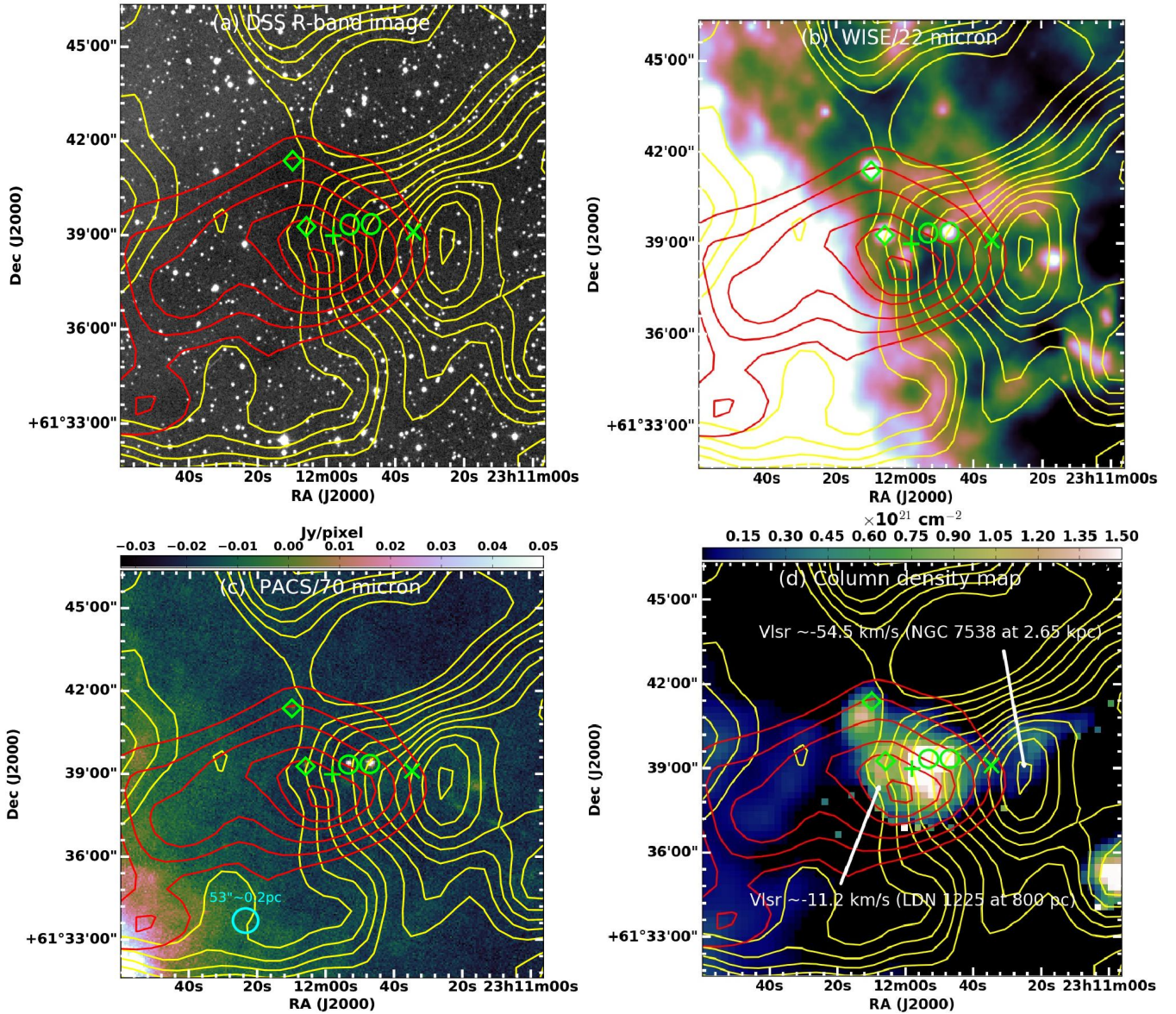


**Figure 12.** Locations of the  $70\ \mu\text{m}$  sources (circles) and the distributions of moment 0 maps of two  $^{12}\text{CO}$  gas components overlaid on multi-wavelength images: (a) DSS R-band image, (b) WISE  $22\ \mu\text{m}$  image, (c) *Herschel*/PACS  $70\ \mu\text{m}$  image, and (d) column density map. Red contours, drawn at 6, 10, 14, 18, 20, and 22  $\text{K km s}^{-1}$ , correspond to  $^{12}\text{CO}$  moment map of LDN 1225 with mean  $V_{\text{LSR}} -11.2\ \text{km s}^{-1}$ . Yellow contours, drawn at 6, 10, 14, 18, 25, 30, 35, 40, 45, 50, and 55  $\text{K km s}^{-1}$ , correspond to  $^{12}\text{CO}$  moment map of distant star forming region in Perseus arm with mean  $V_{\text{LSR}} -54.5\ \text{km s}^{-1}$ . Two bright MIR sources, denoted with diamond symbols, are faint in  $70\ \mu\text{m}$  image. Cloud center of LDN 1225 is denoted with a plus symbol. Location of IRAS 23094+6122 source is shown with a cross symbol. Beam size ( $53'' \simeq 0.2\ \text{pc}$ ) of the CO map is shown with a cyan circle in panel (c). The centers of the CO moment 0 emission peaks of two cloud components are shown with arrows in panel (d). Color bar in panels (c) and (d) correspond to the flux units of the respective image. At  $22\ \mu\text{m}$  image (panel b), the SE region of LDN 1225 has a significant amount of contamination from the background star-forming region NGC 7538.

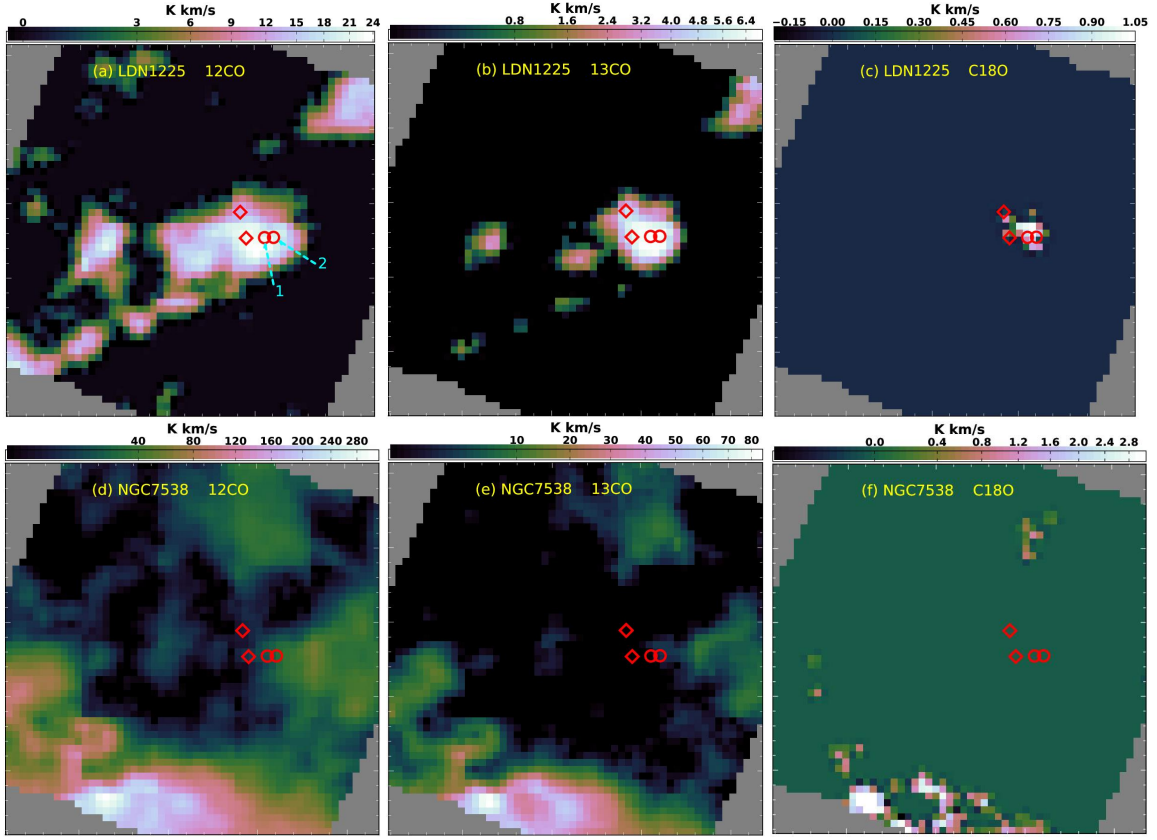


**Figure 13.** The  $^{12}\text{CO}$  (left),  $^{13}\text{CO}$  (middle), and  $\text{C}^{18}\text{O}$  (right) moment 0 maps of the LDN 1225 (panels (a), (b), and (c)) and background/NGC 7538 cloud (panels (d), (e), and (f)). Locations of MIR (diamonds) and  $70\ \mu\text{m}$  (circles) sources are shown. Cyan arrows in panel (a) represent the id numbers of  $70\ \mu\text{m}$  sources. Color bar in each panel corresponds to the pixel values ( $\text{K km s}^{-1}$ ). Coordinates and dimensions of the maps are same as that of Figure 11. North is up and east is to the left.

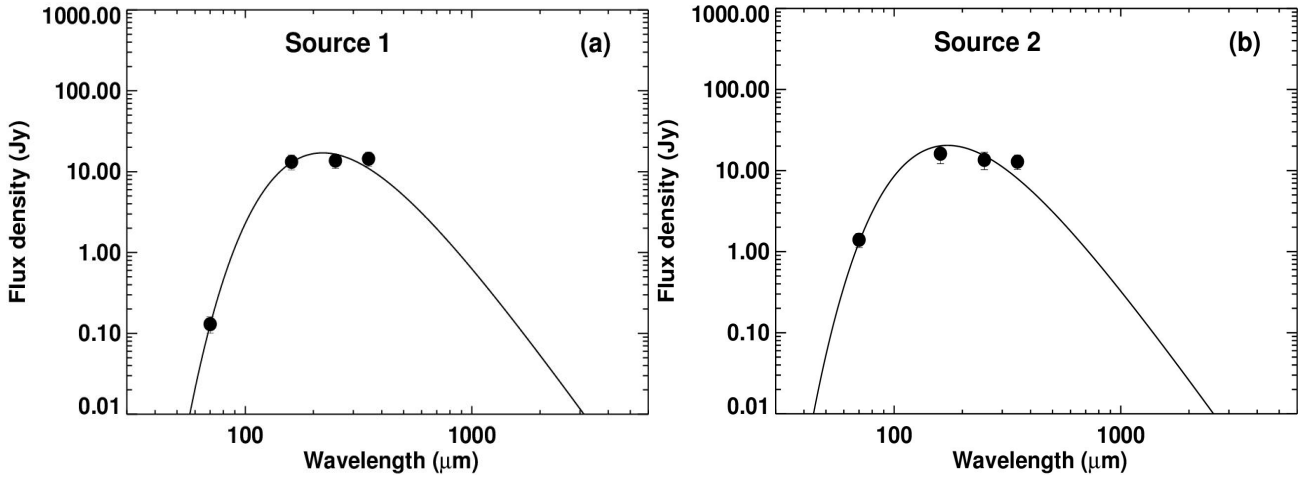


**Figure 14.** The SEDs of envelopes of two  $70\ \mu\text{m}$  sources. Black line shows the best modified blackbody fit to the input fluxes (filled circles) between  $70 - 350\ \mu\text{m}$ . Panels (a) & (b) correspond to the sources 1 & 2, respectively (id numbers are shown in Figure 13(a)).

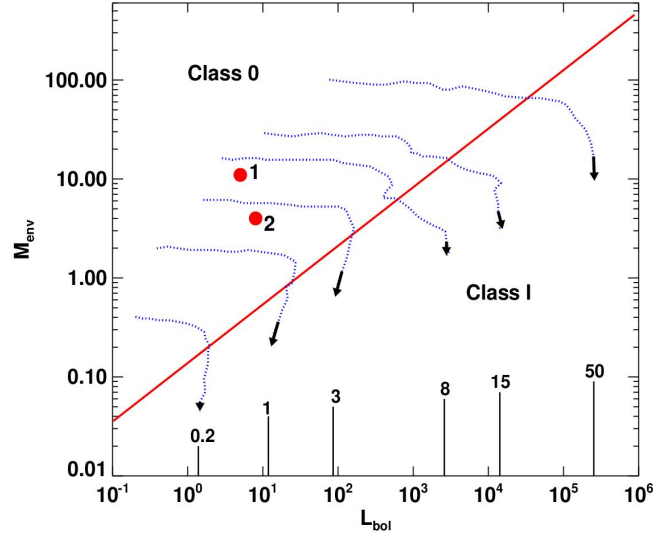


**Figure 15.** Bolometric luminosity ( $L_{bol}$ ) vs. envelope mass ( $M_{env}$ ) for the two  $70\mu\text{m}$  sources (filled circles with IDs). The dotted blue lines represent the evolutionary tracks from [André et al \(2008\)](#). Evolution proceeds from the upper left to the lower right (depicted with arrows at the end of each track). The final stellar masses of these tracks in solar units are given above the lower axis. The slanted red line corresponds to the location where 50% of the initial core mass is converted into stellar mass (see [Bontemps et al 1996](#); [Andre et al 2000](#)).

**Table 7.** Total extinction  $A_V$  values of 57 stars derived using NIR extinction method. ID numbers, coordinates, NIR colors, and polarization values are also given.

ID	RA (J2000)	Dec (J2000)	$[J-H]$	$[H-K_S]$	$P_R$	$A_V$
(1)	(2)	(3)	(4)	(5)	(6)	(7)
05	23:10:43.502	61:31:52.251	$0.40 \pm 0.04$	$0.08 \pm 0.04$	$1.8 \pm 0.5$	$0.4 \pm 0.5$
12	23:10:54.662	61:32:45.974	$0.52 \pm 0.04$	$0.22 \pm 0.05$	$2.7 \pm 0.7$	$2.8 \pm 0.6$
15	23:10:56.201	61:31:54.080	$0.26 \pm 0.05$	$0.16 \pm 0.07$	$1.5 \pm 0.5$	$2.5 \pm 0.8$
19	23:11:00.097	61:33:54.450	$0.43 \pm 0.05$	$0.12 \pm 0.05$	$2.5 \pm 0.7$	$1.0 \pm 0.6$
20	23:11:03.445	61:41:30.120	$0.39 \pm 0.04$	$0.08 \pm 0.04$	$2.3 \pm 0.2$	$0.4 \pm 0.5$
42	23:11:18.675	61:46:42.571	$0.42 \pm 0.04$	$0.17 \pm 0.04$	$1.9 \pm 0.3$	$2.2 \pm 0.4$
44	23:11:20.161	61:31:08.886	$0.41 \pm 0.04$	$0.11 \pm 0.05$	$1.8 \pm 0.4$	$0.8 \pm 0.6$
46	23:11:23.872	61:34:43.075	$0.57 \pm 0.04$	$0.16 \pm 0.04$	$2.1 \pm 0.2$	$1.3 \pm 0.5$
47	23:11:24.807	61:31:16.078	$0.47 \pm 0.04$	$0.11 \pm 0.05$	$3.5 \pm 0.8$	$0.8 \pm 0.6$
51	23:11:27.976	61:43:49.180	$0.37 \pm 0.03$	$0.08 \pm 0.04$	$1.5 \pm 0.2$	$0.3 \pm 0.5$
54	23:11:31.673	61:34:05.188	$0.19 \pm 0.04$	$0.08 \pm 0.04$	$3.2 \pm 0.2$	$0.7 \pm 0.5$
55	23:11:32.560	61:33:12.301	$0.34 \pm 0.04$	$0.14 \pm 0.05$	$3.9 \pm 0.6$	$1.7 \pm 0.5$
57	23:11:33.231	61:32:13.758	$0.31 \pm 0.03$	$0.07 \pm 0.04$	$1.3 \pm 0.2$	$0.4 \pm 0.4$
58	23:11:33.251	61:43:31.011	$0.29 \pm 0.04$	$0.10 \pm 0.04$	$1.5 \pm 0.2$	$0.9 \pm 0.4$
59	23:11:34.034	61:45:52.336	$0.36 \pm 0.04$	$0.21 \pm 0.05$	$2.6 \pm 0.6$	$3.2 \pm 0.6$

NOTE—ID numbers are same as those of Table 2.

NOTE—A portion of the table is given here, and the entire table will be available in the online version of the paper.



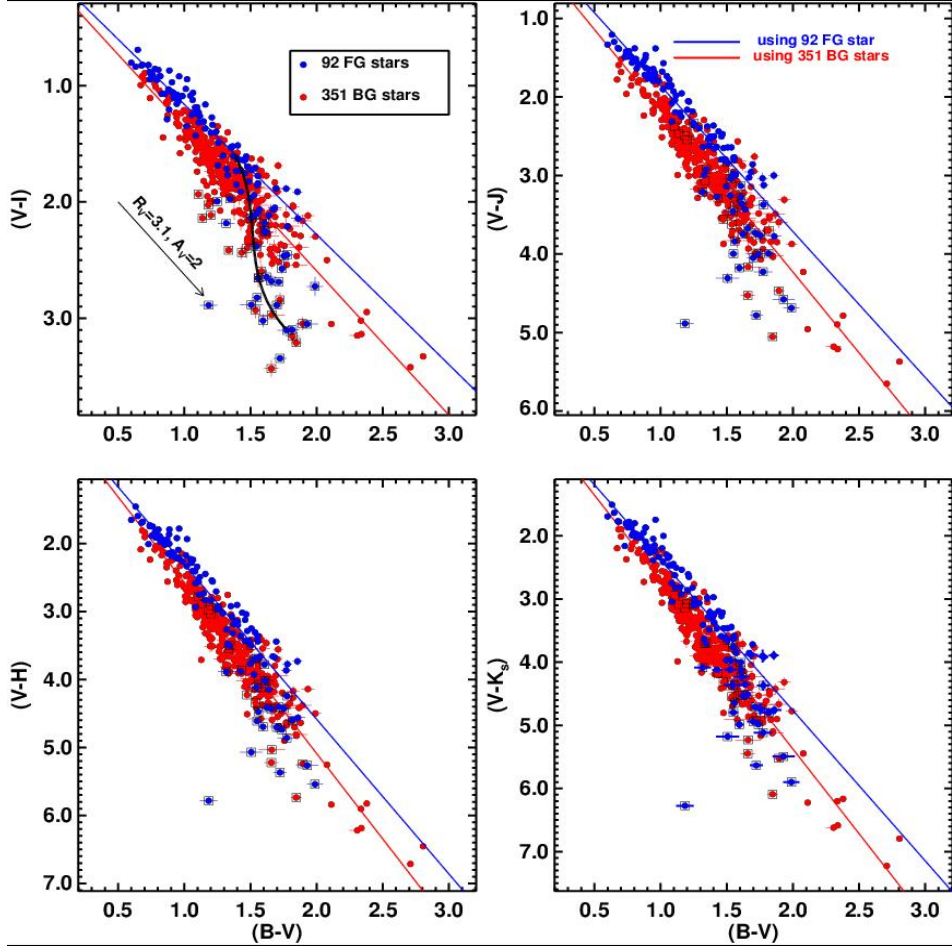


**Figure 16.** The  $(V-I)$ ,  $(V-J)$ ,  $(V-H)$ ,  $(V-K_s)$  versus  $(B-V)$  two-color diagrams of group I stars having distances and photometric data (with uncertainties  $< 0.1$  mag in  $BVIJHK_s$ -bands). The blue and red filled circles correspond to the photometric colors of 92 FG and 351 BG stars, respectively. The blue and red lines corresponds to the weighted linear fits made on the color-color slopes of the FG and BG stars, respectively. The curve in  $(V-I)$  vs  $(B-V)$  represents the locus of the M-type dwarfs (Peterson et al 1998). M-type 27 FG and 16 BG dwarfs, shown with squares, are not used in the fits. The reddening vector representing a normal reddening law ( $R_V = 3.1$ ) is drawn with  $A_V = 2$  mag in the top left panel.

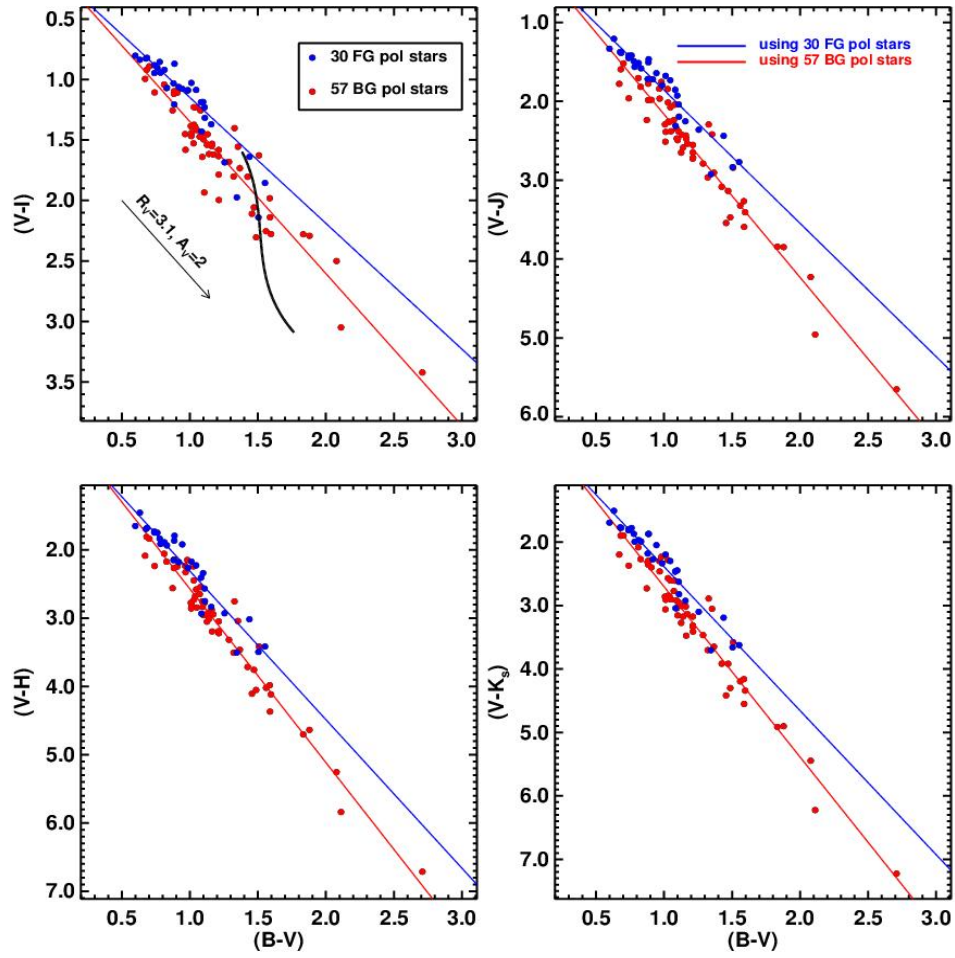


**Figure 17.**  $(V-I)$ ,  $(V-J)$ ,  $(V-H)$ ,  $(V-K_s)$  versus  $(B-V)$  two-color diagrams of the group II stars having polarization, distance, and photometric data (uncertainties  $< 0.1$  mag in  $BVIJHK_s$ -bands). Blue and red filled circles correspond to the photometric colors of 30 FG and 57 BG stars, respectively. The blue and red lines corresponds to the weighted linear fits made on the color-color slopes of the FG and BG stars, respectively. The thick curve in  $(V-I)$  vs  $(B-V)$  represents the locus of the M-type dwarfs (Peterson et al 1998). The reddening vector representing a normal reddening law ( $R_V = 3.1$ ) is drawn with  $A_V = 2$  mag in the top left panel.

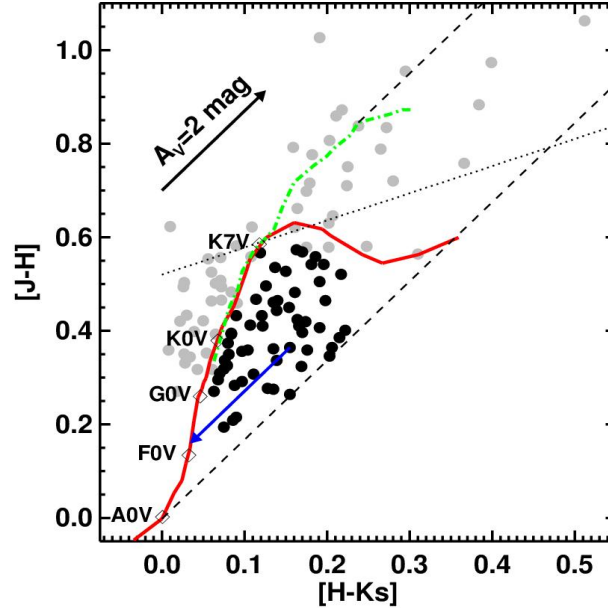


**Figure 18.** NIR color-color diagram of the 113 stars having both polarization and NIR colors. Of these, 57 stars shown with filled black circles have  $(J - K_s) \leq 0.75$  mag and are used to estimate the extinction ( $A_V$ ) values by dereddening their observed  $(J - H)$  and  $(H - K_s)$  colors. Rest of the 56 stars, shown with filled gray circles, are either distributed left side to the locus of the unreddened MS stars and giants, and the stars having  $(J - K_s) > 0.75$  mag (M-type stars or giants). These stars were not used for estimating  $A_V$  values. Blue vector depicts the extinction value of  $A_V = 1.92$  mag derived for a star with an ID 89 (cf., Table 7), whose colors are dereddened using the NIR extinction method. The red curve and green dot-dashed lines represent the unreddened MS and giant branch (Bessell & Brett 1988), respectively. Location of the stars with different spectral types are identified on the MS locus. The dotted line indicates the locus of unreddened CTTSs. The parallel dashed lines are the reddening vectors drawn from the tip (spectral type M4) of the giant branch (left reddening line) and from the base (spectral type A0) of the MS branch. A reference reddening vector with  $A_V = 2$  mag is shown in the upper left portion.

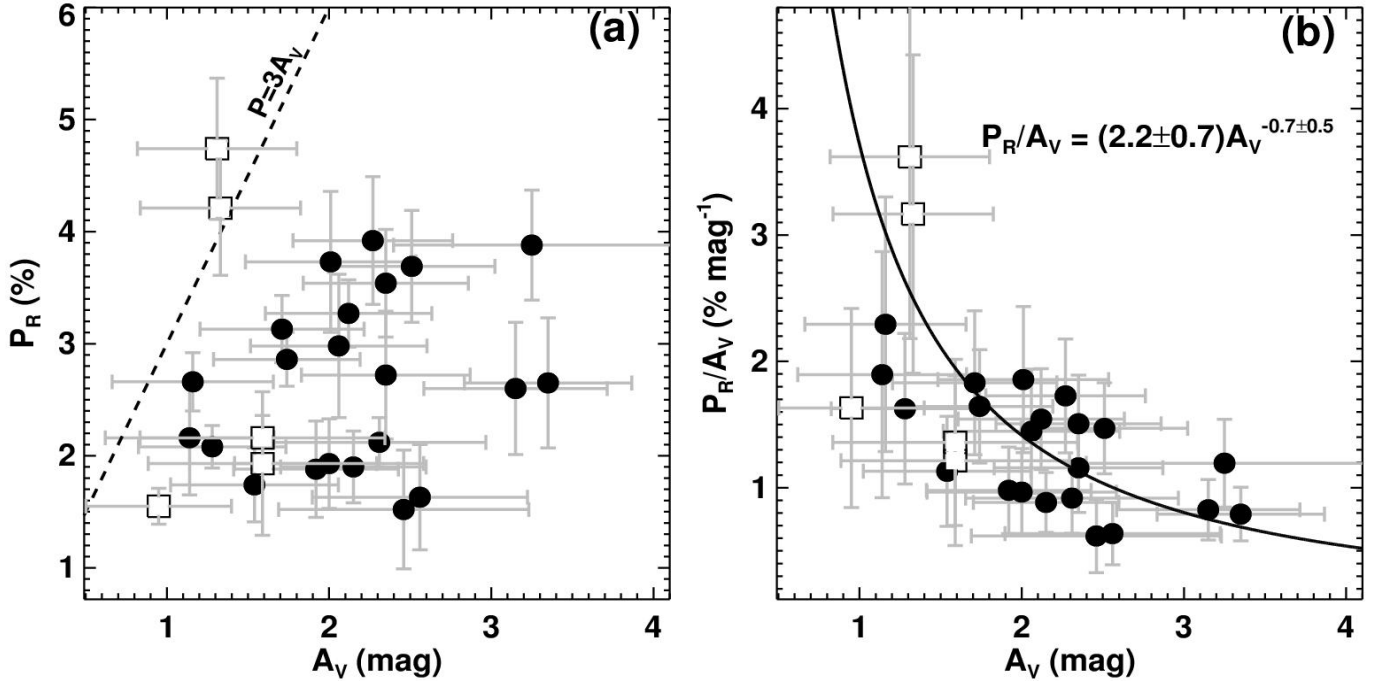


**Figure 19.** (a) Extinction ( $A_V$ ) versus polarization ( $P_R$ ) plot for the 27 stars located towards LDN 1225 and satisfying the criteria  $(J-K_s) \leq 0.75$  mag and  $A_V/\sigma_{A_V} > 2$  (see Appendix B). Dashed line denotes the observed polarization upper limit  $P/A_V = 3$  (% mag $^{-1}$ ) (Serkowski et al 1975) corresponds to the optimum dust grain alignment in the general ISM. (b) Same as (a) but for polarization efficiency diagram, the  $A_V$  versus  $P_R/A_V$ . The 22 BG stars with distances  $> 830$  pc, represented with filled circles, are used in the weighted power-law fit as shown with a thick curve. The resultant fit values are quoted in the plot. It is to be noted here that, of the 27, 3 FG stars having distances  $< 830$  pc and  $P_R < 2.5\%$ , and 2 BG stars distributed above the line  $P = 3 \times A_V$ , as depicted with open squares (in both panels (a) and (b)), are not used in the weighted power-law fit performed in panel (b).